Unique g-C$_3$N$_4$/PDI-g-C$_3$N$_4$ homojunction with synergistic piezo-photocatalytic effect for aquatic contaminant control and H$_2$O$_2$ generation under visible light

Rongdi Tang [a], Daoxin Gong [a,*], Yaoyu Zhou [a,*], Yaocheng Deng [a,*], Chengyang Feng [b], Sheng Xiong [a], Ying Huang [a], Guanwei Peng [a], Ling Li [a]

[a] *College of Resources & Environment, Hunan Agricultural University, Changsha 410128, China*
[b] *KAUST Catalysis Center, Physical Sciences and Engineering Division, King Abdullah University of Science and Technology, Thuwal 23955-6900, Saudi Arabia*

ARTICLE INFO

ABSTRACT

Herein, a g-C$_3$N$_4$/PDI-g-C$_3$N$_4$ homojunction has been fabricated for piezo-photocatalytic atrazine removal and exhibited better performance than individual photocatalysis or piezocatalysis. The introduction of PDI induces the π-π interaction facilitating electrons migration, and twists the g-C$_3$N$_4$ plane into a more polar porous structure with enhanced piezoelectricity. The homojunction facilitates the photoelectron transfer at the g-C$_3$N$_4$/PDI-g-C$_3$N$_4$ interfaces. The photoelectricity and the piezoelectricity of g-C$_3$N$_4$/PDI-g-C$_3$N$_4$ were assessed. The finite element simulation showed that the porous structure of the g-C$_3$N$_4$/PDI-g-C$_3$N$_4$ is essential to the enhanced piezoelectricity. Astonishingly, the piezo-photocatalytic atrazine degradation rate under an optimized condition (pH=2.97) reached 94% within 60 min. Moreover, the g-C$_3$N$_4$/PDI-g-C$_3$N$_4$ homojunction produced 625.54 μM H$_2$O$_2$ during the one-hour piezo-photocatalysis. Given the quenching experiments, reactive species detection and the electronic band of g-C$_3$N$_4$/PDI-g-C$_3$N$_4$, the piezo-photocatalytic mechanism has been proposed. In addition, the degradation pathways and the reduced intermediates toxicity intermediates of atrazine have been investigated.

1. Introduction

With the in-depth development of the modern agricultural industry, the abuse of herbicides, especially atrazine (ATZ), has arisen severe environmental problems. Given the highly stabled structure [1], atrazine is hardly degraded by microorganisms, therefore has caused severe leakage in the groundwater, and even induced a great health risk to humans and other life [2]. Since its toxicity and refractory properties, it is classified as a persistent toxic chemical pollutant by the UNEP (United Nations Environment Programme). Hitherto, strategies including adsorption [3], advanced oxidation processes [4], and photocatalysis have been conducted to remove the atrazine [5–7]. Thereinto, adsorption can only remove the ATZ, while not able to decompose it to reduce the toxicity; the advanced oxidation process commonly introduces other chemicals such as sulfate, ferric salts, which may induce secondary pollution to the environment. Thus, photocatalysis is considered an ideal strategy for atrazine degradation. On one hand, photocatalysis is an economical and environmentally-friendly mode that can directly convert light into electric energy or chemical energy. On the other hand, photocatalytic degradation can effectively mineralize ATZ, rather than simply removing it from the water environment [8,9]. However, given the rapid recombination of the photoinduced electrons and holes, although many efforts have been made on innovating the photocatalysts, the photocatalytic efficiency for the refractory contaminant is still severely suppressed [10,11]. Therefore, developing new strategies to boost photocatalytic efficiency is essential to make a breakthrough in photocatalysis [10].

Recently, many efforts have been made to couple photocatalysis with piezocatalysis and have achieved great progress in water splitting and contaminant degradation [12,13]. During a piezocatalytic process, the external mechanical stress can induce the polarization in the piezocatalyst, leading to the piezoelectric potential in a non-centrosymmetric (NCS) structured crystal, and therefore achieve the catalysis [14]. When combined with photocatalysis, on one hand, the piezo-induced inconsecutive electronic states between the water and the catalyst can provide the driving force for electrons transfer through the solid-liquid

interface [14,15]. On the other hand, the NCS structure of the piezo-catalyst can produce a large polarization field within the catalyst, and therefore boost the directional movement of electrons to weaken pho-togenerated electrons and holes recombination [16]. In previous studies, many materials with intrinsic piezoelectricity, including ferroelectric $BaTiO_3$ [17], two-dimensional ZnS [15], and odd atomic layered centrosymmetric material MoS_2 [18], have been developed for piezo-catalysis. While these materials generally contain metal elements, which may also induce metal leaching and bring secondary pollution during the catalytic process. Fortunately, in a piezocatalysis study of graphene, it was found that introducing polar groups or the nanoscale triangular-shaped holes can induce its asymmetric atom arrangement, and therefore endue piezoelectricity in the inherently nonpiezoelectric graphene [19]. A later study regarding the piezocatalysis of the ultrathin g-C_3N_4 also confirmed the possibility to modify an inherently non-piezoelectric material and endue it piezoelectricity [15].

Considering the visible-light responsive property and the possible piezoelectricity of the g-C_3N_4, increasing its polarity is a promising strategy to enhance its piezoelectricity for simultaneous piezo-photocatalysis. With the rigid π-electron plane, pyromellitic diimide (PDI) is one of the most attractive composites for g-C_3N_4 modification [20]. The PDI can not only provide an aromatic plane to interact with the triazine rings of g-C_3N_4 and induces strengthened π-π interaction [21–23], but also change the plane structure of the layered g-C_3N_4 to induce the plane distortion, arising the enhanced polarization in the material, and therefore resulting in the piezoelectric response [24]. To further promote the photocatalytic efficiency of PDI-modified g-C_3N_4, constructing a homojunction on the basis of the PDI-g-C_3N_4 is also efficient in further facilitating the charge transfer in the catalyst. Recently, more researchers have found that homojunction may offer better interfacial charge transfer efficiency than heterojunction [25]. Li et al. reported that compared to a heterojunction, the same component between the homojunction is likely to promote the continuity of the band bonding, and therefore facilitate the charge transfers through the homojunction interface [26]. Wang et al. reported that an atomically matched α–β phase homojunction in Ga_2O_3 effectively prolonged the photogenerated charges [27]. Such atomic-coherent TiO_2-based homo-junction has been also reported to have good interfacial charge transfer efficiency [28]. Besides, more studies on the g-C_3N_4-based homo-junction, van der Waals $MoSe_2$ homojunction, and $WO_3 @W_{18}O_{49}$ have confirmed that the more consecutive band bending in the homojunction can greatly enhance the migration of photo-electrons [25,29,30]. Considering the environmental compatibility, simple preparation, and fabrication cost, a homojunction consisting of g-C_3N_4 and PDI-g-C_3N_4 with earth-abundant elements is desirable for the piezo-photocatalysis.

Therefore, a unique g-C_3N_4/PDI-g-C_3N_4 homojunction has been fabricated via a facile thermal condensation method to piezo-photocatalytic degrade ATZ and shown great enhancement than barely piezocatalysis and photocatalysis. The g-C_3N_4/PDI-g-C_3N_4 homojunction can induce an enhanced polarization and π-π interaction to promote the piezocatalysis property and facilitate the charge transfer. The piezoelectricity was confirmed via piezoresponse force microscopy (PFM) and the finite element method (FEM) simulation. The photo-catalytic property was evaluated by the electrical chemical workstation. Besides, the g-C_3N_4/PDI-g-C_3N_4 homojunction can also produce H_2O_2 during piezo-photocatalysis. Serials quenching experiments and char-acterizations have been carried out to detect the effective reactive sub-stances generated in the process. In addition, the intermediates and the pathways of ATZ degradation were assessed by tandem mass spec-trometry (LC-MS). Hopefully, the investigation of such a novel homo-junction and its piezo-enhanced photocatalytic performance can inspire more innovation in environmental governance.

2. Experimental section

2.1. Characterization

The morphology was investigated by scanning electron microscopy (SEM, Zeiss Sigma HD, 5.0 kV scanning voltage), transmission electron microscopy (TEM, Titan G260–300, 200 kV scanning voltage), and energy-dispersive X-ray spectrometer (EDX). The porous structure was analyzed via N_2 adsorption-desorption isotherm (Quanta chrome, Autosorb IQ, 325 °C degassing). The crystal structure and the functional groups were investigated by X-ray diffraction (XRD) (Bruker D8 advance, Cu-Kα radiation, 10°/min scanning rate) and Fourier trans-forms infrared spectrometer (FT-IR, Thermo Fisher Nicolet iS5), respectively. The sample surface chemical state was analyzed via X-ray photoelectron spectra (XPS, Thermo Fischer EscaLab Xi+). The elemental analysis was conducted by the elemental analyzer (EA, Ele-mentar Vario EL III). The light absorbance and the photocarrier recombination were evaluated by ultraviolet−visible diffused reflec-tance spectra (UV−vis DRS, UV−vis−NIR spectrophotometer, Hitachi, U4100), Photoluminescence emission spectroscopy (PL, fluorescence spectrometer, Hitachi, F-700), and time-resolved transient photo-luminescence spectra (TRPL, Fluorescence Spectrometers, FLS980). The reactive species generated during the experiment were investigated by electron spin resonance spectra (ESR, Bruker ER200D-SRC spectrom-eter). The mineralization effect was studied by total organic carbon (TOC, Shimadzu, TOC-L).

The photoelectrochemical characterization of the samples was investigated by CHI 660D workstation, with a three-electrode model consisting of Ag/AgCl electrode, Pt electrode, and a working electrode. The lighting conditions of the photoelectrochemical tests were the same as the photocatalyst experiment. To prepare a working electrode, 10 mg photocatalysts were dispersed evenly in 1 mL 0.5% Nafion solution and 1 mL ethanol by the ultrasonic cleaner. Then 100 μL of the above mixed suspension was dropped and dried on a 1 cm × 2 cm FTO slice with a 1 cm^2 effective working area. Finally, the photoelectrochemical mea-surement was conducted in the 0.2 M Na_2SO_4 electrolyte solution.

2.2. Catalysis preparation

All chemicals were analytic purity and obtained from Aladdin Biochemical Technology Co., Ltd. without any pretreatment if not spe-cifically mentioned.

2.2.1. Synthesis of g-C_3N_4
The g-C_3N_4 nanosheet was prepared via a two-step thermal condensation of urea [31]. To obtain the bulk g-C_3N_4, 10 g urea was placed in a covered ceramic crucible and heated to 550 °C (with 1 °C/min heating rate) for 4 h in a muffle furnace under a static air. After cooling to the room temperature, the bulk g-C_3N_4 was ground and heated to 500 °C (with 5 °C/min heating rate) for 2 h under the same condition, and then naturally cool down to room temperature to form a nanosheet structure.

2.2.2. Synthesis of PDI-g-C_3N_4
A one-step thermal condensation was applied to fabricate PDI-g-C_3N_4. Firstly, the mixture of 10 g pyromellitic dianhydride (PMDA) and 1 g as-prepared g-C_3N_4, heated to 325 °C (with 7 °C/min heating rate), and maintained 4 h in a muffle furnace [32–34]. After natural cooling, the obtained sample was grounded and washed by boiled ultrapure water to remove the un-reacted monomers. Then, the resulting PDI-g-C_3N_4 was dried at 60 °C for 12 h under vacuum, noted as PC.

2.2.3. Synthesis of g-C_3N_4/PDI-g-C_3N_4 homojunction
The CNPC homojunction was prepared by condensing PDI-g-C_3N_4 and g-C_3N_4. At first, 5 g PDI-g-C_3N_4 and g-C_3N_4 mixture (with a certain ratio) were mixed. Then, the mixed powder underwent a four-hour

thermal condensation under 325 °C after 7 °C/min heating. Finally, the obtained pale yellow g-C$_3$N$_4$/PDI-g-C$_3$N$_4$ powder was collected and labeled with CNPC1, CNPC2, CNPC3, CNPC4, CNPC5, where the PDI-g-C$_3$N$_4$: g-C$_3$N$_4$ mixture ratio was 1:4, 1:2, 1:1, 2:1, and 4:1, respectively.

2.3. Piezo-photocatalytic performance

To investigate the piezo-photocatalytic efficiency of the synthesized catalysts, an ultrasonic cleaner (40 kHz, 200 W, Beauty, Kunshan, China) and a Xe lamp (300 W, PLS-SXW300D, Beijing Perfectlight, China) with a 420 nm cut filter were applied. The reactor is 20 cm away from the lamp. Firstly, 30 mg prepared sample was added into ATZ solution (50 mL, 10 ppm). After stirring 20 min in a dark environment for complete adsorption, the suspension was placed in an ultrasonic cleaner under visible light for 1 h. During the process, solutions were acquired at different times and filtered to monitor the ATZ concentration change via high-performance liquid chromatography (HPLC), eluted by methanol (70%) and ultrapure water (30%).

To evaluate H$_2$O$_2$ production, iodine titration was applied [35]. Generally, 30 mg catalyst was dispersed in 50 mL ultrapure water. During the process, 1 mL reaction solution was obtained and filtered at a specific reaction time (10, 20, 40, 60 min). Then 1 mL 0.1 M C$_8$H$_5$KO$_4$ solution and 1 mL 0.4 M KI solution were added to the reaction solution, immediately. Once the C$_8$H$_5$KO$_4$ and KI solution was added, the produced H$_2$O$_2$ in the solution will immediately react with the I^- to produce I_3^-, which arises a strong absorption peak at 350 nm allowing quantification of the H$_2$O$_2$. After 20 min complete reaction, the solution absorption at 350 nm was estimated by a UV–vis spectrometer (Shimazu, UV-1700). Moreover, serials quenching experiments and LC-MS were carried out to study the catalytic mechanism and the ATZ degradation intermediates and pathways.

3. Results and discussion

3.1. Construction of the homojunction

The fabrication and the proposed molecular structure of the CNPC piezo-photocatalysts are shown in Fig. 1A and Fig. S1. The layered structure of the as-prepared g-C$_3$N$_4$ can be observed in the SEM image (Fig. 1B). After the later condensation processes, the framework was still maintained in PDI-g-C$_3$N$_4$ and the CNPC composites, and a more porous structure was shown on the sheet (Fig. 1C-D). Such change was also
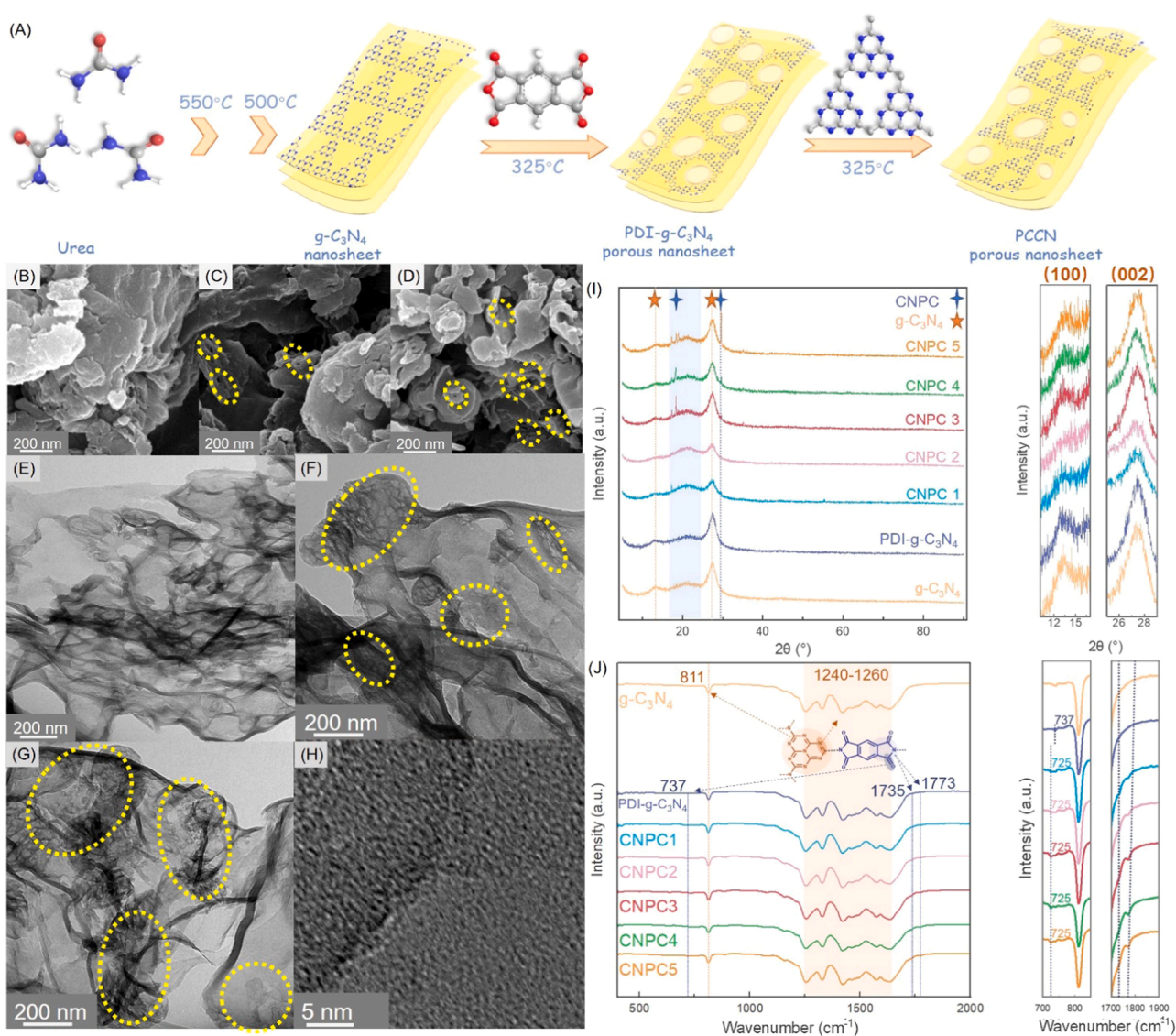

Fig. 1. (A) The synthetic route of the catalysts. SEM image of the (B) g-C$_3$N$_4$, (C) PDI-g-C$_3$N$_4$, and (D) CNPC-3; TEM image of the (E) g-C$_3$N$_4$, (F) PDI-g-C$_3$N$_4$, and (G) CNPC-3; (H) HR-TEM image of CNPC3. (I) XRD patterns and (J) FT-IR spectra of the catalysts.

verified via the TEM image (Fig. 1E-G). Under the 325 ℃ condensations of the PDI-g-C₃N₄, the addition of the PMDA and further condensation of amino groups can induce the generation of H_2O and NH_3 gas [32], which may act as a gaseous template and leads to the more porous structure in PDI-g-C₃N₄, and the CNPC homojunction [36]. The evenly elemental distribution in the CNPC3 suggests that the PDI-g-C₃N₄ and g-C₃N₄ were well-condensed (Fig. S2). Fig. 1H shows the high-resolution TEM image of CNPC3, its highly amorphous structure is similar to the g-C₃N₄.

Fig. 1I shows the XRD pattern and the enlarged peaks of the prepared sample. The (100) peak at 13.2° and the (002) peak at 27.7°, originating from the in-planar and interlayered heptazine in g-C₃N₄, were observed in all samples. These peaks in PDI-g-C₃N₄ showed weaker intensity and positive movement with a higher 2θ value, since the PDI units in CNPC twists the layered structure of the pristine g-C₃N₄ and induces a thinner, smaller nanosheet, and decreased interlayer stacking along the (100) and (002) direction [15,24]. Compared with PDI-g-C₃N₄, the above-mentioned change became more obvious in all the CNPC samples. Besides, there are new sharp peaks with different intensities shown in the range of 15–30° in CNPC composites, implying that further calcinating the mixture of PDI-g-C₃N₄ and g-C₃N₄ can induce the synthesis of new species and the regulated crystallinity [32]. Specifically, the peaks

at 2θ = 18.4°, 29.5°, and 35.1° in CNPC samples were assigned to the π-π interaction between the g-C₃N₄ and PDI, which can induce the π-π * electron delocalization between the conjugated aromatic units of CNPC, and therefore boost the intermolecular charge transfer [32].

In the Fourier transforms infrared (FT-IR) spectra (Fig. 1J), typical bands between 1250 and 1650 cm⁻¹ and the peak at 811 cm⁻¹ are the stretching vibration of aromatic C-N rings and triazine ring in g-C₃N₄, respectively [37]. These peaks can be found in all the fabricated catalysts, indicating that the well-preservation of the graphitized structure framework in the homojunction. While in the PDI-g-C₃N₄, three characteristic peaks of the bending vibration, symmetric stretching, and asymmetric stretching of imide carbonyl groups are shown at around 737, 1735, and 1773 cm⁻¹, respectively [32]. Notably, in all the CNPC samples, the bending vibration of imide carbonyl groups was negatively moved to 725 cm⁻¹ for the inductive effect caused by the strong electron-donating amino group and the generation of a stronger conjugation in the homojunction [38].

The inner porous structure of the catalysts was invested via the N_2 adsorption-desorption isotherm (Fig. 2A). All the samples showed the IV-type isotherm-induced hysteresis loops, indicating their mesoporous-dominated structure [39]. Fig. 2B shows the Barrett-Joyner-Halenda
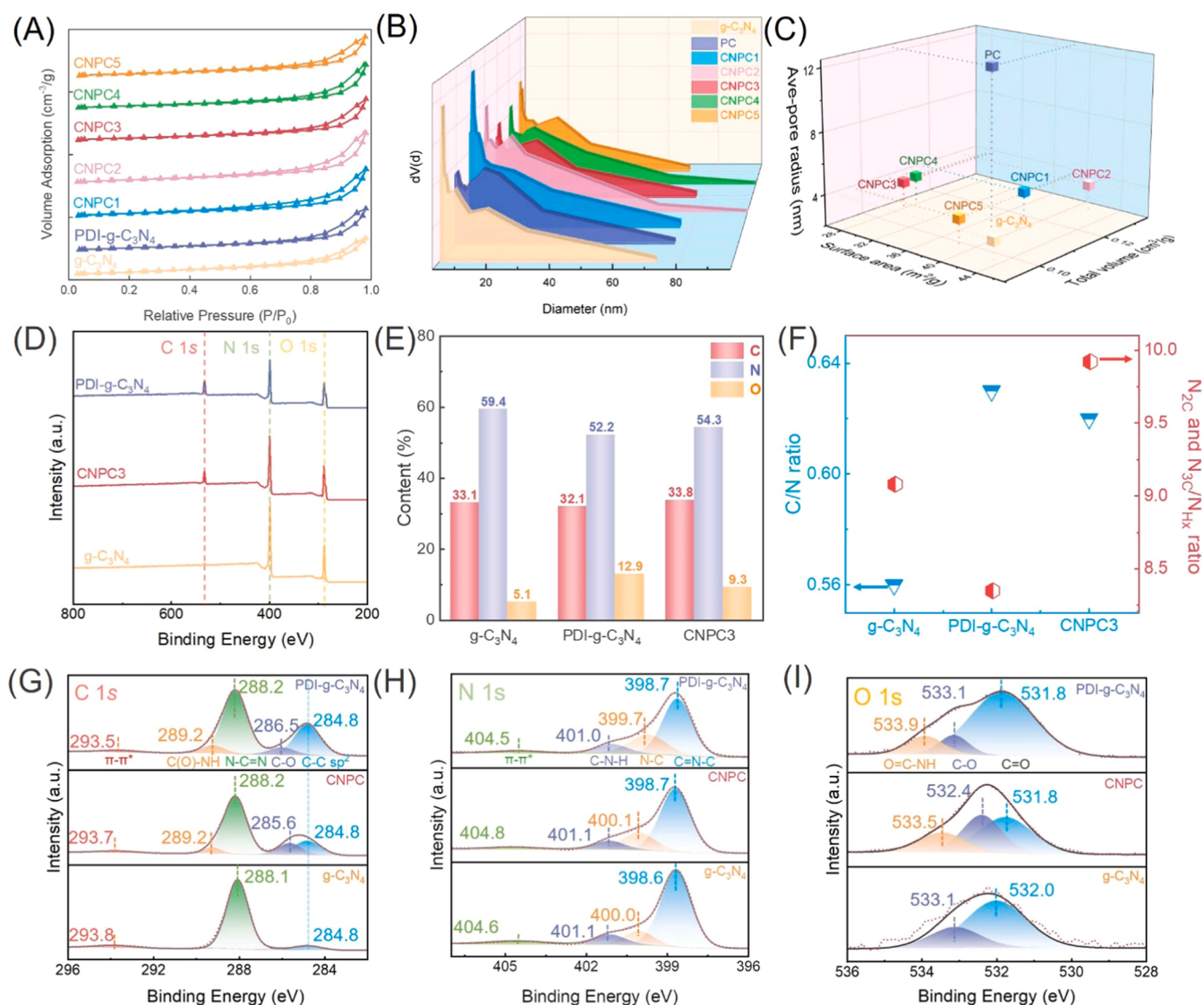

Fig. 2. (A) The N_2 adsorption-desorption isotherms, (B) pore radius information, and (C) the detailed pore structure and the SSA of the as-synthesized composites; (D) The XPS survey spectra, (E) elemental contents, (F) C/N and $N_{2\,C}$ and $N_{3\,C}/N_{Hx}$ ratio, (G) the C 1s, (H) the N 1s, and (I) the O 1s spectra of the g-C₃N₄, PDI-g-C₃N₄, and CNPC3.

(BJH) methods that analyzed the pore diameter of the catalysts. The pore diameter of g-C$_3$N$_4$ is mainly distributed at 3.8 nm. While in the PDI-g-C$_3$N$_4$ sample, a wide BJH peak was shown at around 12.3 nm, which can be explained by the twisted layer structure and the narrowed interlayer spacing in PDI-g-C$_3$N$_4$. The twisted structure can induce the non-centralized distribution of pore size [24], which is essential for enhancing the polarization of the catalyst. When the PDI-g-C$_3$N$_4$ hybridized with g-C$_3$N$_4$, the sharp peak at around 3.8 nm and the wide peak with a larger diameter were simultaneously shown in all CNPC samples. The more detailed pore structure information is summarized in Fig. 2C. Compared with other samples, the g-C$_3$N$_4$ owns a slightly smaller total pore volume (0.09 cm^3/g) and a bit larger specific surface area (SSA) (44.70 m^2/g). The SSA and total volume difference between the PDI-C$_3$N$_4$ and g-C$_3$N$_4$ were not obvious. However, when further condensed them to synthesis CNPC samples, the surface area of CNPC3 and CNPC4 was dramatically reduced to 28 m^2/g, and the total volume of CNPC1 and CNPC2 was increased a little to 0.12–0.13 cm^3/g. As previously speculated, the synthesis of CNPC can induce a smaller nanosheet and decreased interlayer distances, leading to the reduced SSA. Also, the enhanced polycondensation degree and the close contact between the PDI-g-C$_3$N$_4$ and g-C$_3$N$_4$ are likely to induce decreases in SSA and the increase in the pore volume [40]. The decreased SSA and the interlayer space in the CNPC are possible to further enhance the π-π interaction and thereby facilitate the electrons transfer [33].

X-ray photoelectron spectroscopy (XPS) was applied to further investigate the chemical state and the elemental composition of the catalysts. Fig. 2D-E exhibit the XPS survey spectra and the elementary composition of each catalyst analyzed by EA. The as-prepared g-C$_3$N$_4$ mainly consisted of C and N, and the 5.1% O was probably the adsorbed water and the carbon dioxide [41]. In the PDI-g-C$_3$N$_4$ and CNPC3, the increased O percentage was attributed to the introduction of PDI. The atomic ratio of C to N, and the sum of sp^2 C=N-C (N$_{2\,C}$) and sp^3 N-C (N$_{3\,C}$) to N-H (N$_{Hx}$) in these catalysts were calculated (Fig. 2F). The C/N of g-C$_3$N$_4$ was 0.56, and increased to 0.63 and 0.62 in PDI-g-C$_3$N$_4$ and CNPC3, respectively. The increased C/N of these catalysts indicates the deepening of condensation degree and release of NH$_3$ during the synthesis. Comparing g-C$_3$N$_4$ and PDI-g-C$_3$N$_4$, The N$_{2\,C}$ and N$_{3\,C}$/N$_{Hx}$ atomic ratio in CNPC was the highest, indicating the most aromatic N and the least NH$_2$ contents. This is mainly attributed to the further condensation of the terminal NH$_2$, heptazine rings and the triazine rings in the g-C$_3$N$_4$ and PDI-g-C$_3$N$_4$, which may offer a more conjugated structure to facilitate the electrons transfer. While the lower N$_{2\,C}$ and N$_{3\,C}$/N$_{Hx}$ in PDI-g-C$_3$N$_4$ than g-C$_3$N$_4$ might be arisen from the generation of amino groups by C-N bonds breaking of PMDA during the synthesis of PDI-g-C$_3$N$_4$ [15]. Fig. 2G-I shows the high-resolution XPS, and all the peaks were corrected by the sp^2 C (284.8 eV). As shown in the C 1s spectra (Fig. 2G), the sharp and strong peak of g-C$_3$N$_4$ located at 288.1 eV is the C that bonded with three N (N-C=N), whereas the weak peak at 284.8 eV is assigned to the C-C sp^2. The highest energy contribution at 293.8 eV is assigned to the π-π*electronic transition of the conjugated systems [42]. These peaks are also shown in the C 1 s spectra of PDI-g-C$_3$N$_4$ and g-C$_3$N$_4$. Besides, two new peaks of the C-O and C (O)-NH (289.2 eV) are formed because of the existence of PDI. The N 1 s spectra of the as-prepared samples are similar, consisting of C=N-C (around 398.7 eV), N-C (around 400.0 eV), C-N-H (around 401.1 eV), and the π-π * (around 404.5 eV) (Fig. 2H). The O 1s spectra of g-C$_3$N$_4$ are made up of C=O (532.0 eV) and C-O (533.1 eV) (Fig. 2I). After decorating PDI, a new O=C-NH peak formed at 533.9 eV in PDI-g-C$_3$N$_4$. In the CNPC homojunction, these three O peaks are also shown with slightly lower binding energy, which can be attributed to the partial decomposition of the bonded O during the thermal condensation process [43].

3.2. Photoelectrical and piezoelectric analysis

To study the photoelectrical attribute of g-C$_3$N$_4$, PDI-g-C$_3$N$_4$, and the

CNPC, their steady-state photoluminescence (PL) emission spectra, TRPL spectra, electrochemical impedance spectroscopy (EIS), photocurrent response, and Linear sweep voltammetry (LSV) were measured (Fig. 3). According to the PL spectra that reflect electron separation efficiency (Fig. 3A), the peak intensity for g-C$_3$N$_4$ was extremely strong, even exceeding the signal detect threshold, implying its high recombination rate [44]. With the PDI decoration, the increased π-π conjugated system between the PDI and g-C$_3$N$_4$ facilitates the long-range electron migration, thus the signal was partially quenched in PDI-g-C$_3$N$_4$. With the reduced recombination of electrons and holes by homojunction, the signal was further lowered in the CNPC. The transient fluorescence spectrometer was also applied to investigate the TRPL spectra of the catalysts (Fig. 3B). The g-C$_3$N$_4$, PDI-g-C$_3$N$_4$, and the CNPC3 all have biexponential functional radiative lifetime decay. The biexponential function parameters of each catalyst are shown in Fig. 3B, calculated via Eqs.1–2 [45].

$$I(t) = A_1 \exp\left(-\frac{t}{\tau_1}\right) + A_2 \exp\left(-\frac{t}{\tau_2}\right) \tag{1}$$

$$\tau_A = \frac{A_1\tau_1^2 + A_2\tau_2^2}{A_1\tau_1 + A_2\tau_2} \tag{2}$$

Where the τ_1, τ_2, and τ_A are respectively the short, long, and the average fluorescent lifetime, A_1 and A_2 are the weight factor of the short and long fluorescent lifetime.

The τ_1 and τ_2 of g-C$_3$N$_4$ were the highest and its τ_A reached 7.35 ns. Thanks to the enhanced π-π conjugation in PDI-g-C$_3$N$_4$, its τ_1 and τ_2 all decreased than the pristine g-C$_3$N$_4$, with its τ_A reduced to only 4.17 ns. With the construction of the homojunction in the CNPC, the τ_A value was further dropped to 4.12 ns. The decrease of the average fluorescent lifetime in the PDI-g-C$_3$N$_4$ and CNPC homojunction should be beneficial from the more effective non-radioactive decay path that originated from the better electron delocalization in the π-π conjugation and their boosted transfer in the homojunction [7,45]. Therefore, the recombination of photocarrier in the CNPC homojunction can be efficiently inhibited, which is following the PL results. The electrochemical impedance spectroscopy (EIS) Nyquist plots in Fig. 3C revealed that the PDI-g-C$_3$N$_4$ displays a much smaller diameter than bare g-C$_3$N$_4$, for the PDI induced π-π conjugated system gives reduced recombination efficiency. The diameter of the CNPC homojunction was further reduced because the charge transfer was further promoted by the homojunction-induced built-in electric field within [41]. The transient photocurrent response of the samples was measured (Fig. 3D). With visible light, the g-C$_3$N$_4$ exhibited the weakest current response, while the photocurrent responses in the PDI-g-C$_3$N$_4$ were enhanced for the π-π interaction facilitates the electrons transfer. With the homojunction and the enhanced condensation degree, the photocurrent response of CNPC3 was further increased. Specifically, the CNPC homojunction showed a distinct photocurrent decay upon the light illumination, implying the fast recombination of the photoexcited electrons and holes [46,47]. Even though, the CNPC still showed the best photocurrent response when reaching a steady-state (Fig. S3). The linear sweep voltammetry (LSV) shows the photocurrent density order of CNPC3 > PDI-g-C$_3$N$_4$ > g-C$_3$N$_4$, following the above results (Fig. 3E) [48,49]. To further analyze the optical properties of the catalysts, UV–vis DRS was performed. In the DRS spectra (Fig. 3F), the curve intensity of the PDI-g-C$_3$N$_4$ was the highest, while the g-C$_3$N$_4$ showed the lowest absorption intensity. Based on the light absorption intensity of the CNPC samples, an interesting rule can be concluded from the DRS spectra of the samples: the more PDI-g-C$_3$N$_4$ contents, the higher the light absorption intensity. This could benefit from the pale-yellow color of the PDI-g-C$_3$N$_4$. Based on the DRS information of the catalysts, their Tauc plots were plotted according to the equation below [50,51].

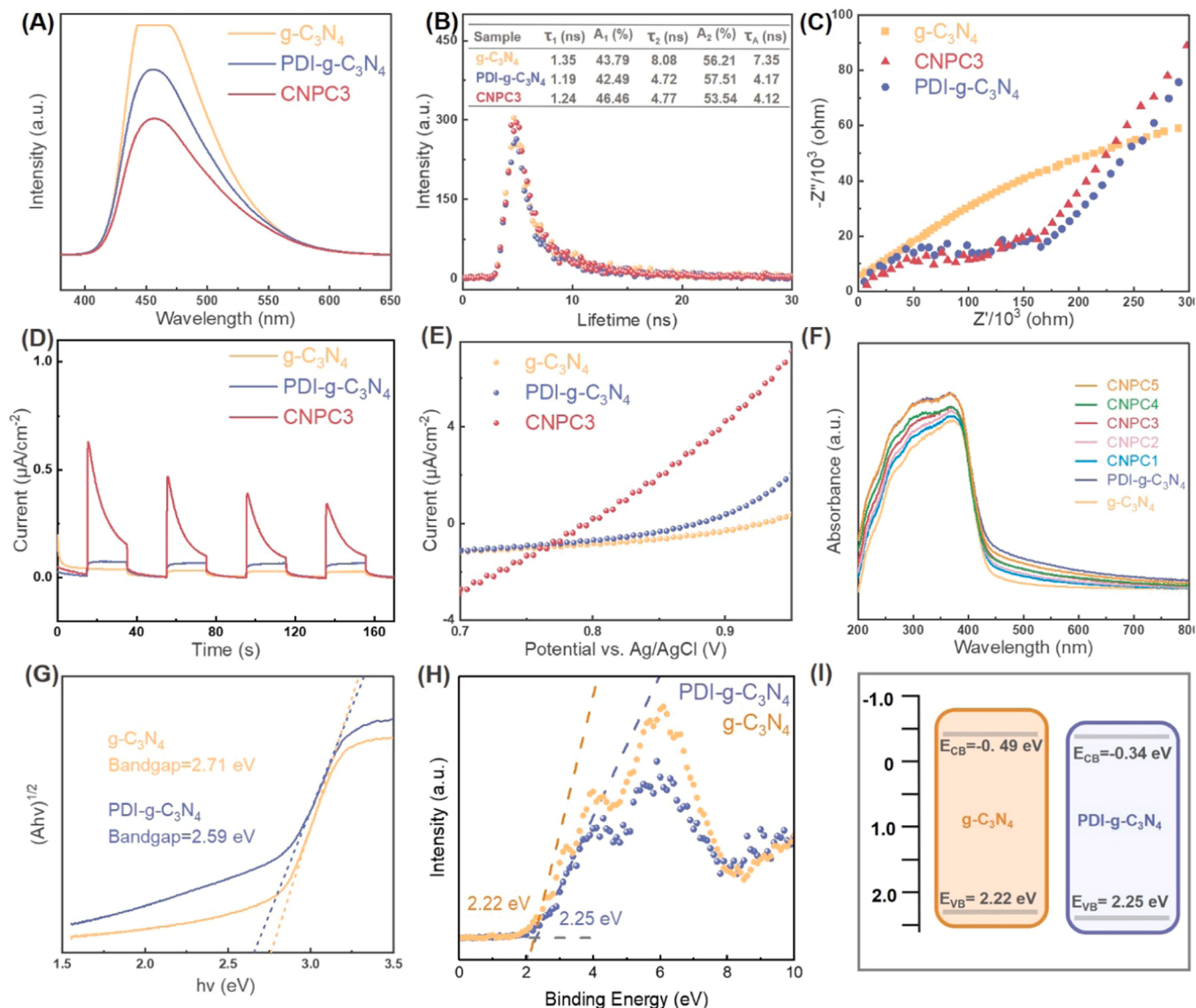$$\alpha h\nu = A\left(h\nu - E_g\right)^{\frac{1}{2}} \tag{3}$$

Fig. 3. The photoelectricity of the catalysts. (A)The PL spectra, (B) TRPL spectra, (C) EIS Nyquist plots, (D) transient photocurrent response, (E) the LSV, (F) the DRS spectra, and (G) the Tauc plots of the g-C$_3$N$_4$ and PDI-g-C$_3$N$_4$; the valence band potential of (H) g-C$_3$N$_4$ and PDI-g-C$_3$N$_4$, and (I) their electronic band configurations.

Where α, h, ν, A E_g respectively are the absorption coefficient, Planck constant, light frequency, and bandgap energy.

As shown in Fig. 3G, the E_g of g-C$_3$N$_4$ is the largest, estimated to be 2.71 eV, in accordance with the previous studies [52,53]. While after introducing PDI, the bandgap of PDI-g-C$_3$N$_4$ was largely reduced (2.59 eV) for its higher light absorption edge. Hence the introduction of PDI-g-C$_3$N$_4$ to the homojunction is very important for increasing the utilization of light and better the electrons excitation. The Mott-Schottky curves of the g-C$_3$N$_4$, PDI-g-C$_3$N$_4$, and CNPC3 with negative slope are shown in Fig. S4, indicating they are all n-type semiconductors [41]. To further understand the electronic band configuration of the CNPC homojunction, the VB potential (E_{VB}) of g-C$_3$N$_4$ and PDI-g-C$_3$N$_4$ were respectively 2.22 and 2.25 eV, determined by the valence band (VB) spectra (Fig. 3H). Given the E_{VB} and E_g of the samples, the conduction band (CB) potential (E_{CB}) of the samples can be determined by the following equation.

$$E_{CB} = E_{VB} - E_g \qquad (4)$$

Thus, the E_{CB} of the g-C$_3$N$_4$ and PDI-g-C$_3$N$_4$ are figured out to be − 0.49 eV and − 0.35 eV for each. The electron configurations of the

CNPC were described in Fig, 3I. Apparently, the lower E_{CB} in PDI- g-C$_3$N$_4$ is likely to boost the electron directional migration from g-C$_3$N$_4$. Meanwhile, the higher E_{VB} position of g-C$_3$N$_4$ in the homojunction is favorable to accumulate the holes from PDI-g-C$_3$N$_4$, and therefore boost the electrons and holes separation, simultaneously [54].

The piezoelectricity of CNPC catalysts was investigated by PFM. According to the deflection image and the topology image from PFM (Fig. 4A and Fig. S5A), approximately 10 layered CNPC with a total height of around 50–60 nm is clearly observed. Fig. S5B-C shows a clear piezo potential and phase difference on the CNPC surface when the AFM tip is scanning across the sample. The difference of the phase and amplitude in different regions implies the distinguished polarization degree and polarization direction [17,55,56]. Interestingly, it is obvious that the thinner portion of the sample can induce a higher potential and greater phase change. This could be one of the reasons for the enhanced piezo-photocatalytic efficiency of CNPC. The phase-voltage and displacement-voltage plots are shown in Fig. 4B-C. Under the external electric field, the piezoelectricity of the CNPC leads to a 130°-phase-difference in the hysteresis loop, and a maximum of 1-nm-displacement of the sample [15]. During the piezo-photocatalysis process, the air bubble absorbs the acoustic energy and continuously grows with the
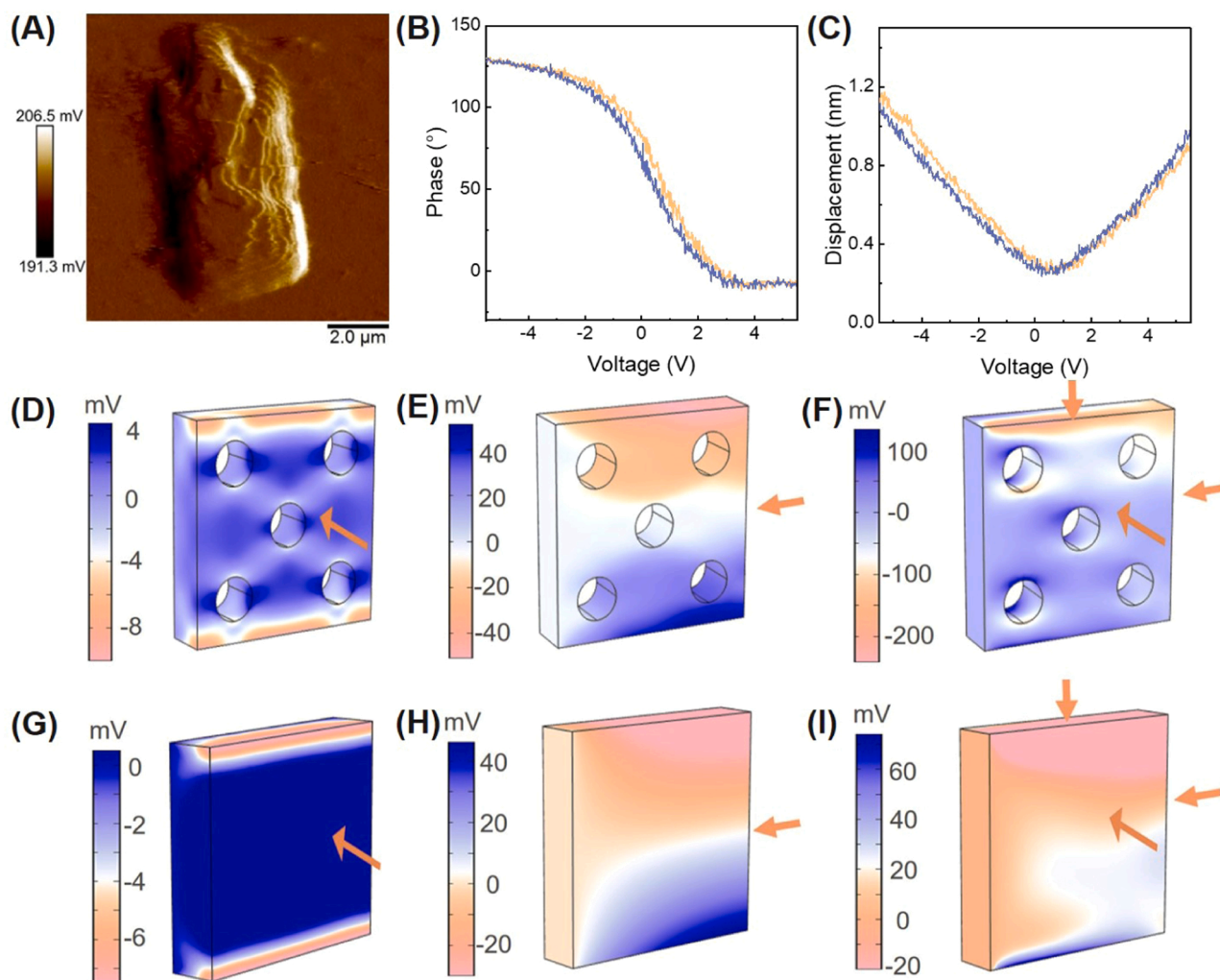
Fig. 4. The piezoelectricity of the CNPC catalyst. (A) The stacked CNPC sheet; (B) phase–voltage, and (C) displacement–voltage curve studied via piezoresponse force microscopy; the FEM simulation demonstrates the piezoelectric potential distribution of a size of 50 * 50 * 10 nm (D-F) porous CNPC sheet or (G-I) the g-C$_3$N$_4$ sheet with a 10 MPa sonication-induced pressure from different directions.

solution vibration. When the accumulated energy exceeds the threshold, the bubbles collapse and produce high pressure (10 MPa) on the catalyst [56], leading to the dipole polarization charge and built-in electric field in the catalysts [57]. Such inner piezo potential is variable with the strength and the direction of the strain and will keep existing until the external stress vanished [13,57]. To further investigate the enhanced piezoelectricity of CNPC than g-C$_3$N$_4$, the FEM by COMSOL Multiphysics was applied to simulate their piezoelectric effect. The models of porous and smooth nanosheet with 50 * 50 * 10 nm size were constructed to simulate the porous CNPC nanosheet (Fig. 4D-F), and the g-C$_3$N$_4$ nanosheet (Fig. 4G-I), respectively. The arrow refers to the direction of 10 MPa pressure. In both g-C$_3$N$_4$ and CNPC, it is obvious that the smaller stressed area produces the bigger piezopotential difference even under the same pressure intensity. When the pressure is imposed from three different directions simultaneously (Fig. 4F and I), the potential difference is largely enhanced by more than one magnitude than a single direction. It is worth noting that no matter where the pressure comes from, the piezo potential difference in the porous CNPC is always more significant than that in g-C$_3$N$_4$. When 10 MPa stress from three directions is applied, more than threefold differences are shown between them [57]. The enhanced potential difference in CNPC illustrates its promoted energy harvest and conversion ability [15]. Moreover, the porous CNPC surface gives more obvious electric fields distributing, which can accelerate the electron-hole pairs separation and migration

upon visible light irradiation [56].

3.3. Piezo-photocatalytic performance

3.3.1. Piezo-photocatalytic atrazine degradation

The photo-piezo catalytic performance of the CNPC homojunction was evaluated by the degradation of ATZ. The degradation of ATZ of the different catalytic systems and the estimated reaction rate constants (k) were shown in Fig. 5A and Fig. S6A. In a dark environment, the ATZ itself barely degraded within 60 min (K=0.0001). Even the CNPC3 was introduced, the ATZ removal was negligible in the absence of the photo or piezo stimulation (K=0.0002). With the piezo-photocatalytic of g-C$_3$N$_4$, 22.0% ATZ removal rate was obtained (K=0.0035), and the ATZ removal was enhanced to 35.6% by PDI-g-C$_3$N$_4$, which was contributed to the enhanced π-π conjugation and the polarity of the composite [32, 33]. CNPC3 exhibited the strongest piezo-photocatalytic catalytic performance, with a significant increase in the ATZ degradation rate to 77.3% with K= 0.0247. The largely increased performance of CNPC than the g-C$_3$N$_4$ and PDI-g-C$_3$N$_4$ mixed powder with the equal ratio (46%, K=0.0096) further indicates the successful construction of the homojunction that facilitates the electron migration and boosted the piezo-photocatalytic efficiency. In addition, the photocatalytic and the piezocatalytic efficiency of CNPC3 were also assessed. With the visible light stimulation, the ATZ degradation by CNPC3 was only 21.9%.
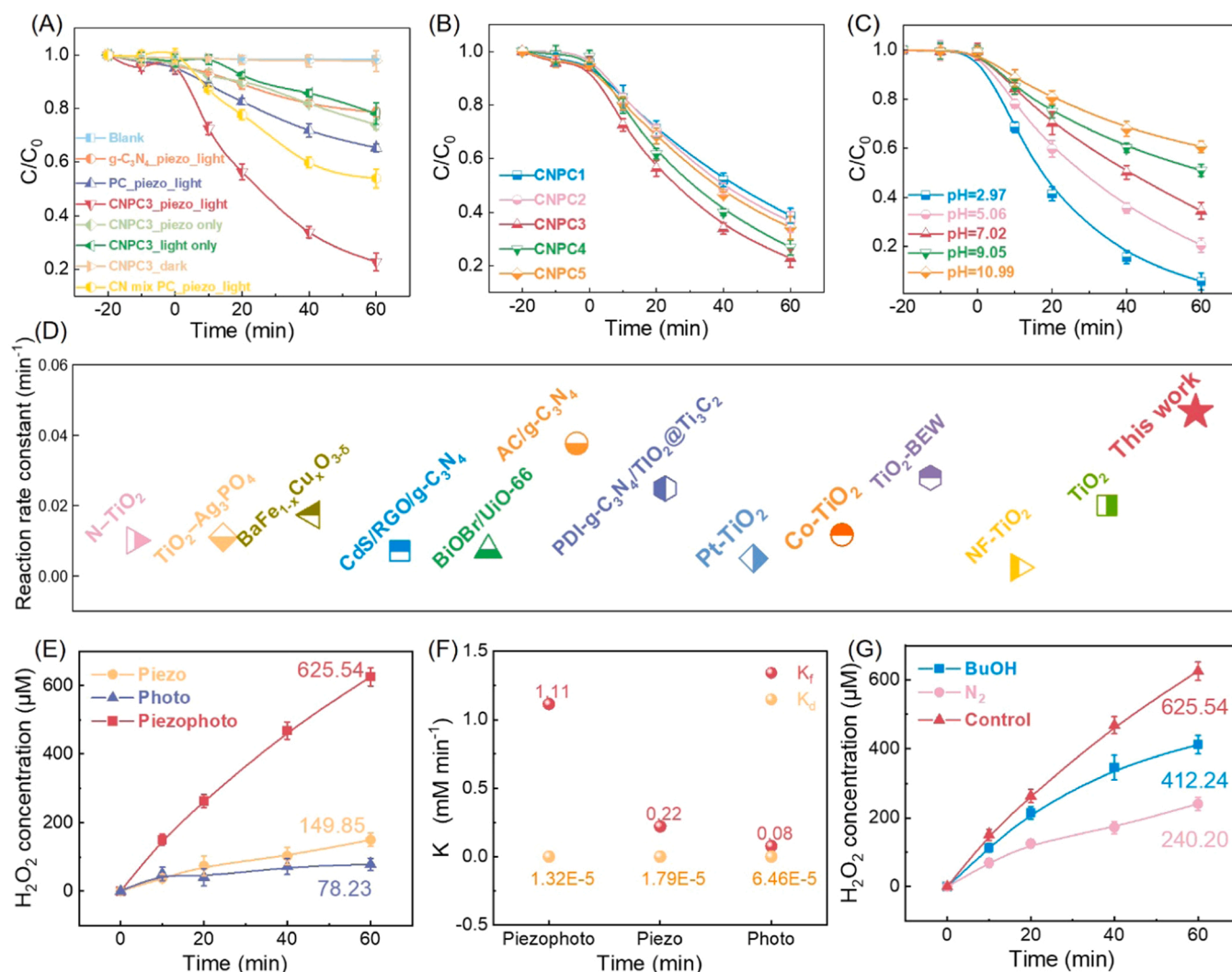
Fig. 5. Piezo-photocatalytic catalytic performance of the CNPC homojunction. (A) the piezo-photocatalytic catalytic ATZ degradation by CNPC; (B) the piezo-photocatalytic catalytic performance of the CNPC homojunction with different g-C_3N_4: PDI- g-C_3N_4 ratio; (C) the influence of the solution pH. (D) The atrazine degradation reaction rate constant comparison between this work and other studies. (E) The piezo-photocatalytic H_2O_2 generation by CNPC3 homojunction; (F) the H_2O_2 formation rate constant (K_f) and the decomposition constant (K_d) by CNPC3 under the different catalytic system; (G) The piezo-photocatalytic H_2O_2 generation by CNPC3 homojunction in N_2 or BuOH solution.

Interestingly, the piezocatalytic degradation of ATZ by CNPC3 raised to 36.0%, even higher than the pure photocatalyst. The better piezocatalytic efficiency than photocatalytic efficiency was previously reported in another piezo-photocatalytic hydrogen production investigation of the g-C_3N_4 [15]. This is probably for the introduction of PDI-g-C_3N_4 in the CNPC homojunction increasing the polarization of the composite. The enhanced polarization electric field in CNPC homojunction boosted the carrier separation and the directional migration of the carriers [10], therefore inducing better piezocatalytic performance than photocatalytic performance in the CNPC3 homojunction [58].

The piezo-photocatalytic ATZ degradation by CNPC homojunction with different g-C_3N_4: PDI-g-C_3N_4 ratios were also evaluated (Fig. 5B and Fig. S6B). All the CNPC homojunction performed better than g-C_3N_4 and PDI-g-C_3N_4, implying the enhanced electron transport of the CNPC homojunction during the piezo-photocatalysis. Interestingly, with the PDI-g-C_3N_4 content increases in CNPC1 to CNPC3, the piezo-photocatalytic performance was gradually increasing; while when the PDI-g-C_3N_4 content further increases, the piezo-photocatalytic performance was then dropped from CNPC3 to CNPC5. Combined with the abovementioned discussion that the light absorbance of the CNPC homojunction increases with the PDI-g-C_3N_4 content, it can be

speculated that the prominent piezo-photocatalytic performance of CNPC3 homojunction was not solely raised from the enhanced light absorption and the narrower bandgap by the PDI-g-C_3N_4, but the synergetic effect between the g-C_3N_4 and PDI-g-C_3N_4. Given the best piezo-photocatalytic atrazine degradation of the CNPC3, the experiments mentioned below were all performed with CNPC3. The reaction system pH has always been considered as the major factor that influences the reaction activity. Thus, the ATZ degradation in the CNPC/piezo-photocatalysis system was performed under pH 2.97–10.99 (Fig. 5C and Fig. S6C). The CNPC/piezo-photocatalysis system showed a brilliant efficiency under a strongly acidic environment (pH=2.97), the piezo-photocatalytic ATZ removal even reached 94%, with K = 0.0466. While the pH increased, the piezo-photocatalytic efficiency kept decreasing. In the ATZ solution with pH = 10.99, the ATZ removal rate of the CNPC/piezo-photocatalysis system dramatically dropped to 40% (K=0.0088). In the previous study, it was found that the photocatalytic activity of PDI may vary with the solution pH value for the stability of the terminal carboxy group on PDI is pH-dependent [59]. In an alkalic environment, the deprotonation of PDI may occur and induce the destruction of the hydrogen bonding between the adjacent carboxy and thus weaken the catalytic performance of the PDI [59]. Besides, the

original pH of the 50 mL 10 ppm ATZ solution was measured to be 6.31, and the corresponding reaction rate constant (k = 0.0247) was situated between that for pH = 5.06 (k = 0.0261) and pH = 7.02 (k = 0.0174), following the above tendency. Notably, under an optimized condition (pH=2.97), the photocatalytic ATZ removal in this CNPC/piezo-photocatalysis system showed a much higher reaction rate constant than many reported studies (Fig. 5D) [3,6,7,60–68].

3.3.2. Piezo-photocatalytic H_2O_2 generation

In our previous study, it was found that the PDI-g-C_3N_4 is likely to produce H_2O_2 during the photocatalytic and thus transform into $\cdot O_2^-$ to further boost the reaction [7]. While the H_2O_2 production is pH-dependent because the H_2O_2 generation is governed by proton-coupled electron transfer [69–72]. The lower pH, the better H_2O_2 production. Therefore, it was possible for CNPC to produce H_2O_2 in the piezo-photocatalytic process and promote reaction efficiency. Subsequently, the production of H_2O_2 was enhanced under an acidic environment and promoted the piezo-photocatalytic degradation by CNPC. To verify this assumption, the H_2O_2 generation in the CNPC/piezo-photocatalysis system with different conditions was also performed (Fig. 5E). Before the tests, the concentration-absorbance standard curve of H_2O_2 was plotted (Fig. S7). Under the solely visible light simulation, only 78.23 μM H_2O_2 was produced within 60 min. The H_2O_2 in piezocatalysis was almost twice that in photocatalyst, reaching 149.85 μM. The higher piezocatalytic than the photocatalytic performance of CNPC is following its trend in Fig. 5 A. In the synergy piezo-photocatalysis, the H_2O_2 generation was dramatically promoted, even reaching 625.54 μM. The H_2O_2 formation with the different catalysts and catalysis process were also evaluated (Fig. S8). Under the same catalytic process, the H_2O_2 generation in the CNPC homojunction was better than g-C_3N_4 and PDI-g-C_3N_4, the same with the ATZ degradation performance tendency. Interestingly, the differences between these catalysts were not obvious when individual photocatalysis and piezo-catalysis were conducted. While the piezo-photocatalytic H_2O_2 generation in the CNPC homojunction was distinctly higher than the g-C_3N_4 and PDI-g-C_3N_4. The introduction of PDI-g-C_3N_4 in the CNPC homo-junction largely enhanced the asymmetry of the molecular structure, which is essential for the polarization in the molecule and thus induces the piezopotential distribution differences. Besides, the enhanced π-π interaction and the construction of homojunction greatly boost the movement of photoelectrons and inhibit their recombination, offering much better utilization of lights [15,29,33]. As a result, the synergistic piezo-photocatalysis H_2O_2 production by the CNPC homojunction is largely promoted than the pristine g-C_3N_4 and PDI-g-C_3N_4.

Generally, the generation of H_2O_2 is accompanied by its decomposition during the reaction. To investigate the H_2O_2 generation in the CNPC/piezo-photocatalysis system, its pseudo-first-order kinetic model of photocatalysis, piezocatalysis, and piezo-photocatalysis were fitted to figure out the H_2O_2 generation reaction constant (K_f) and its decomposition reaction constant (K_d) via Eq. 5. The K_f and K_d under different catalysis are shown in Fig. 5F. Compared with the piezocatalysis or photocatalysis along, piezo-photocatalysis owned the highest K_f (1.11 mM·min^{-1}), and the lowest K_d (1.32*10^{-5} mM·min^{-1}). By contrast, the K_f of H_2O_2 in photocatalysis was the lowest, with the highest K_d. These results insist that the CNPC homojunction has a superior piezocatalytic effect than the photocatalytic effect, and the synergetic piezo-photocatalysis can largely enhance the contaminant removal and H_2O_2 generation performance by CNPC homojunction.

$$[H_2O_2] = \frac{K_f}{K_d}\left(1 - e^{-K_d t}\right) \tag{5}$$

To further investigate the reactive species that influence the piezo-photocatalytic H_2O_2 generation, quenching experiments were carried out by bubbling N_2 gas or adding 10% vol. tertiary butanol (BuOH) as ●OH sacrificial agent in ultrapure water. The H_2O_2 generation with

different conditions over time is shown in Fig. 5 G. After adding 10% BuOH, the H_2O_2 generation was reduced by a third to 414.24 μM within 60 min. While when the dissolve O_2 was driven out by N_2, the H_2O_2 yield was significantly suppressed with only 240.20 μM. These results indicate that both O_2 reduction and ●OH conversion are critical for the H_2O_2 yield.

3.3.3. Practicality evaluation of the CNPC piezo-photocatalyst

To evaluate the piezo-photocatalytic practicality of the CNPC homojunction, serials of environmental simulation experiments were carried out. Fig. 6 A shows ATZ degradation by the CNPC/piezo-photocatalysis system with the existence of citric acid (CA), fulvic acid (FA), and humic acid (HA). Generally, the piezo-photocatalytic degradation performance of ATZ by CNPC increases with the CA increases. With 20 mg/L CA, the degradation of ATZ was basically the same as the general condition (k = 0.0241–0.0247). While when CA concentration raised to 100 mg/L, the ATZ degradation rate constant even reached 0.0293 with an 81% removal rate (Fig. S9A). This may be due to acidic conditions promoting H_2O_2 generation and thus boosting the atrazine degradation [72]. In comparison, both FA and HA showed a slight inhibition effect for the ATZ degradation in this system (Fig. S9B-C). Interestingly, although FA generally suppressed the ATZ degradation in this system, the reaction rate constant increased with the FA increases within the FA concentration of 20–100 mg/L. According to the previous reports, natural organic matter (NOM) has rich phenolic hydroxyl and carboxyl groups. On one hand, these substances are possible to quench the reactive species and inhibit the ATZ degradation process [73]; on the other hand, the phenolic hydroxyl and carboxyl groups are also possible to be activated during the reaction and release ●OH to boost the reaction process. Therefore, the degradation of ATZ fluctuates due to the complex reaction caused by NOMs [1,74]. The influence of coexisting ions has been also assessed (Fig. S9D). The piezo-photocatalytic ATZ degradation was basically steady with the Cl^-, SO_4^{2-}, and NO_3^- co-existing. Specifically, CO_3^{2-} and HCO_3^- greatly suppressed the atrazine degradation to only 14% and 38% for each. Such inhibition effect is possibly attributed to that the alkalinity of CO_3^{2-} and HCO_3^- lead to the reduced stability of PDI that weakened the π-π interaction in the homojunction [59]. To assess the influence of actual water on piezo-photocatalytic ATZ removal, the filtered river water (collected from Liu yang River, at 113°08′74 N 28°17′91 E) and tap water were applied to prepare the 10 ppm ATZ solutions. The piezo-photocatalytic ATZ removal in tap water was slightly decreased to 73% (k = 0.0225). While the ATZ degradation in river water was obviously decayed to only 38% removal rate within 60 min (Fig. 6B). The severely weakened effect could be contributed to the abundant NOM or other substances in the river water. Since the complexity of the river water, it is difficult to identify the specific causes. Fortunately, when the river water prepared ATZ solution was adjusted to pH = 2.86, the piezo-photocatalytic ATZ degradation was greatly enhanced to 64%, which greatly resolved the low ATZ degradation in the natural water body. Such improvement of the ATZ degradation performance could be beneficial from the more H_2O_2 generation in an acidic environment.

The reusability of the photocatalyst was evaluated via cycling reaction and the characterization of the used catalyst. As shown in Fig. 6 C, the ATZ degradation in the CNPC/piezo-photocatalysis system was basically steady after four runs, decreasing to 70% from 78%. The XRD spectra of the fresh and the used CNPC3 are shown in Fig. 6D. Compared to the XRD pattern of the fresh CNPC, the π-π conjugation between the g-C_3N_4 and PDI (at 18.4°, 29.5°, and 35.1°) were well-preserved, indicating the π-π interaction was basically stabled in the catalyst. The peak at 13.2° and 27.7° were also preserved while the 27.7° peak intensity was weakened, implying the decrease of the interlayered heptazine in CNPC. Such a decrease in the intensity of the interlayered heptazine could be originated from the exfoliation of the CNPC homojunction by the ultrasonic during the catalysis [75]. Fortunately, such change in the used catalyst has very little influence on the π-π conjugation system of
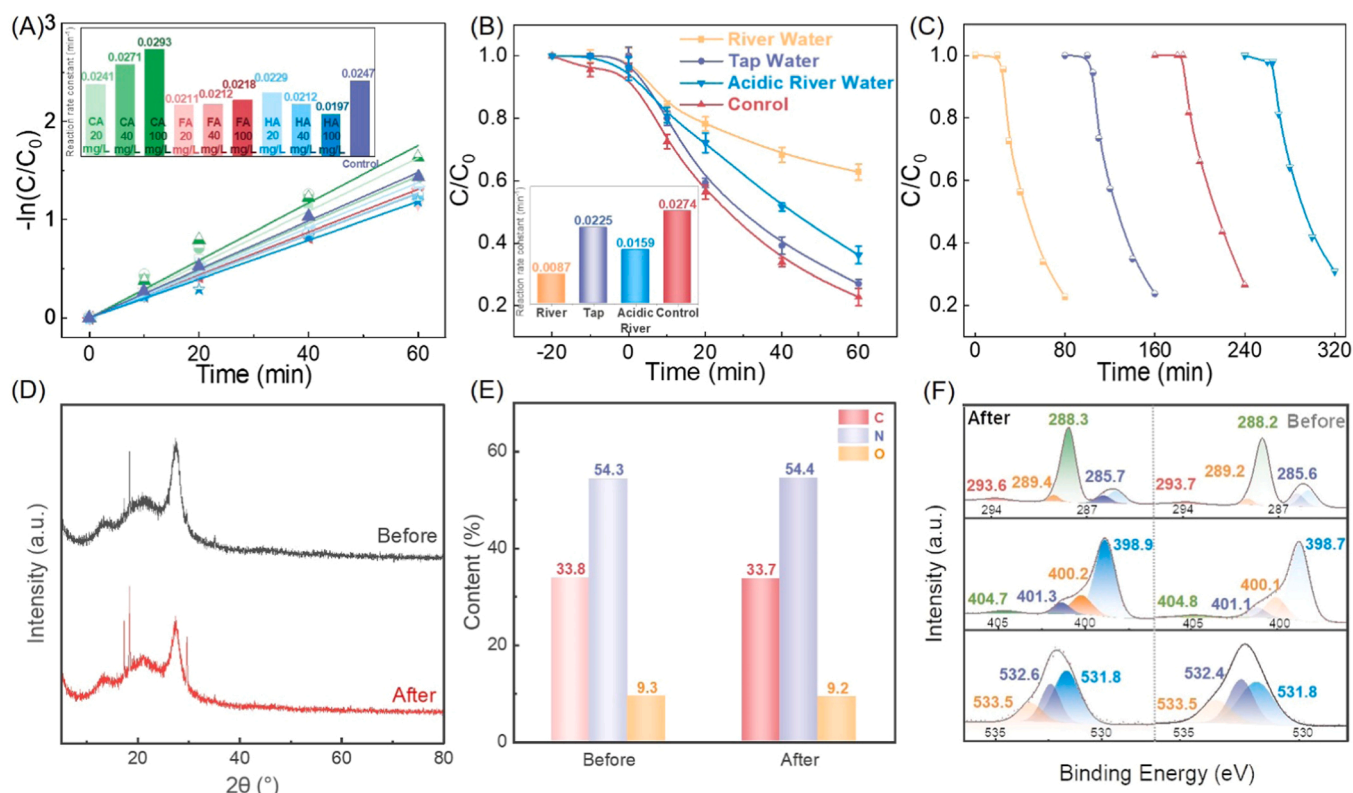
Fig. 6. Practicality evaluation of the CNPC piezo-photocatalyst. (A) The pseudo-first-order kinetic plots of the ATZ degradation with a different organic acid or natural organic matters existence; (B) the ATZ piezo-photocatalytic degradation plots of CNPC with different actual water; (C) the cycling experiments of the CNPC homojunction; (D) the XRD comparison of the fresh and used CNPC homojunction; (E) the atomic ratio of the fresh and the used CNPC homojunction; (F) the XPS narrow spectra comparison of the used and fresh CNPC homojunction.

the catalysts and the cycling performance. The XPS was also carried out to evaluate the surface chemical state differences between the fresh and used CNPC. Fig. 6E shows the different elemental proportions analyzed by EA. After piezo-photocatalysis, the elementary composition in the CNPC homojunction shows no obvious change, indicating the highly stabled structure of the catalyst. Fig. 6 F shows the XPS narrow spectra comparison of the CNPC before and after the catalytic process. Compared with the peaks in fresh CNPC (Fig. 2G-I), the main peak positions were basically unchanged. The majority of C 1 s peaks and the N 1 s were slight positively moved (0.1–0.2 eV) in the used CNPC for the enhanced relative proportion of C and N. Specifically, the π-π*excitation peaks were negatively moved in both C 1s and N 1 s spectra even their enhanced ratio, indicating the slightly weakened π-π interaction. Combined with the weakened interlayered heptazine XRD peak, it is believed that the decreased interlayered heptazine induced a slight loss of π-π conjugation.

3.4. Reaction mechanism study

3.4.1. Reactive substance analysis

To figure out the reactive species for the piezo-photocatalytic ATZ degradation, BuOH, ethylenediaminetetraacetic acid disodium salt (EDTA-2Na), 1,4-Benzoquinone (p-BQ), and furfuryl alcohol (FFA) were applied to quench· • OH, h⁺, ·O_2^-, and $^1O_2$, respectively (Fig. 7A-B) [40, 50,51]. It was found that the effect of the • OH quencher BuOH was relatively weak. When 20 mM BuOH was added to the solution, the ATZ degradation was basically unchanged with 76% removal. With the BuOH concentration continuously increased to 50 mM, the ATZ removal rate showed an obvious decayed to 67%. While the ATZ degradation did not further decrease when the BuOH concentration increased to 100 mM. The impact of BuOH on ATZ degradation indicates the limited

effect of • OH [76], 50 mM BuOH is enough to eliminate most • OH. Comparatively, the EDTA-2Na had a greater influence on ATZ degradation. When the EDTA-2Na concentration increases from 0.5 to 2 mM, the ATZ removal rate significantly decreased from 70% to 46%. Comparatively, p-BQ showed a stronger inhibitory effect. With only 1 mM p-BQ applied, the ATZ removal rate was dramatically decreased to 26% due to the ·O_2^- quenching. And this value further decreases to 22% when the p-BQ concentration rises to 5 mM. Surprisingly, FFA showed the strongest suppression for the piezo-photocatalytic ATZ degradation. Only 1 mM FFA could reduce the ATZ degradation rate to 8%, and the reaction rate constant (k = 0.0018) was more than one-tenth less than the common condition (k = 0.0247). With the FFA raising to 5 mM, the ATZ decomposition almost stopped with only a 4.9% removal rate (Fig. 7B). Based on the above analysis, the reactive substances contribution in this system can be found as $^1O_2 >$ ·$O_2^- >$ h⁺ > • OH.

To further analyze the reactive species generation by CNPC homojunction during the piezo-photocatalyst process, an ESR test was carried out with the existence of ultrasound and visible light (Fig. 7C-D). There was no reactive species signal in the dark environment, while when the ultrasound and visible light were applied, the signal for $^1O_2$, • OH, and ·O_2^- were detected at the 10 min of the piezo-photocatalysis. Considered the redox potential of O_2/·O_2^- (−0.33 eV) and •OH/OH⁻ (1.99 eV) [77, 78], along with the band configuration of the CNPC homojunction, the ATZ degradation and H_2O_2 generation could be elucidated as Eqs. 6–14. During the piezo-photocatalysis, abundant photoelectrons and holes are generated in the CNPC homojunction (Eq. 6). The holes could promote the generation of • OH or O_2 (Eqs. 7–8) [69,79], while the electrons could react with O_2 to generate • O_2^- (Eq. 9) [79], which is important for the H_2O_2 and $^1O_2$ formation (Eqs. 10–11) [80,81]. During the catalysis, the • OH and H_2O_2 are also mutually transformed (Eqs. 12–13) [69]. Finally, all the reactive substances could effectively eliminate ATZ (Eq.
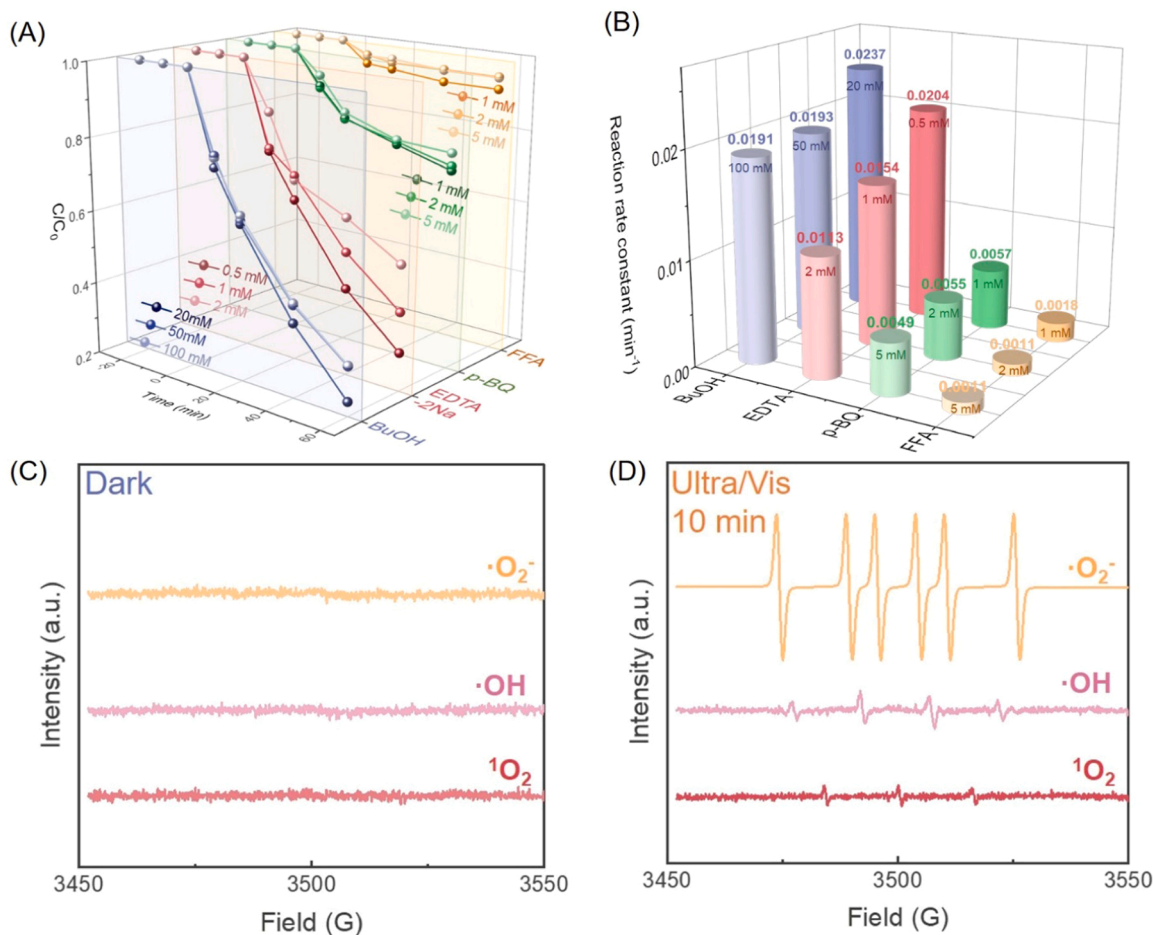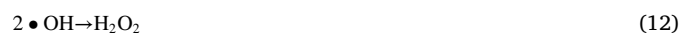
Fig. 7. The reactive species detection. (A) The piezo-photocatalytic ATZ degradation plots with quenching agent existent; (B) the reaction rate constant; the ESR signal of $^1O_2$, •OH, and $\cdot O_2^-$ in (C) dark environment and (D) piezo-photocatalysis.

14).

$$CNPC + h\nu \xrightarrow{Ultrasound} h^+ + e^- \qquad (6)$$

$$OH^- + h^+ \rightarrow \bullet OH \qquad (7)$$

$$2H_2O + 4h^+ \rightarrow O_2 + 4H^+ \qquad (8)$$

$$e^- + O_2 \rightarrow \bullet O_2^- \qquad (9)$$

$$2 \bullet O_2^- + 2H^+ \rightarrow {}^1O_2 + H_2O_2 \qquad (10)$$

$$h^+ + \bullet O_2^- \rightarrow {}^1O_2 \qquad (11)$$

$$2 \bullet OH \rightarrow H_2O_2 \qquad (12)$$

$$H_2O_2 + e^- \rightarrow \bullet OH + OH^- \qquad (13)$$

$${}^1O_2 + \bullet O_2^- + h^+ + \bullet OH + H_2O_2 + ATZ \rightarrow \quad \text{Degradation products} \qquad (14)$$

3.4.2. Piezo-photo coupling effect in the CNPC homojunction

Given the above discussion, the plausible piezo-enhanced photocatalytic mechanism in the CNPC homojunction could be proposed (Scheme 1). In an individual photocatalysis (Scheme 1A), the photocatalytic process obeys a type II heterojunction mechanism. Upon light stimulation, the photogenerated electrons and holes are generated in g-C$_3$N$_4$ and PDI-g-C$_3$N$_4$. Because of the lower VB of g-C$_3$N$_4$ and the higher CB of PDI-g-C$_3$N$_4$, the holes are preferred to accumulate in the VB of g-

C$_3$N$_4$ for oxidation reaction, meanwhile the electrons transport to the CB of PDI-g-C$_3$N$_4$ for the reduction reaction [82]. As the common problem of photocatalysis, the recombination of photoinduced electrons and holes largely hinders photocatalytic performance. During an individual piezocatalysis (Scheme 1B), the ultrasound vibration is contributed to the piezo-potential generation across the homojunction, and therefore drives the directional flow of electrons and induces a build-in piezo-electric field inside the CNPC homojunction [10,15]. Given the chaos of the ultrasonic vibration, the induced piezoelectrical field inside the homojunction is non-directed [15]. The process (a) and (b) in Scheme 1B refer to the alternant opposite piezoelectrical field between the PDI-g-C$_3$N$_4$ and g-C$_3$N$_4$. While at the interfaces between the PDI-g-C$_3$N$_4$ and g-C$_3$N$_4$, it is still possible for partial carries to recombine when the direction of the piezoelectrical field changes, and thus limits the piezocatalytic performance [10].

Thus, there are two possible scenarios in a piezo-photocatalytic process (Scheme 1C). The left image illustrates the piezo-photocatalytic process when the polarization direction points from the g-C$_3$N$_4$ to PDI-g-C$_3$N$_4$, the same as the migration direction of the photogenerated electrons. The build-in piezoelectric field in the CNPC will boost the electrons migration to suppress the photoexcited carrier recombination for the strengthened piezo-photocatalytic performance. While when the polarization direction points from the PDI-g-C$_3$N$_4$ to g-C$_3$N$_4$ (the right image in the Scheme 1C), the piezo-induced built-in electric field was opposite to the direction of the photogenerated electrons, and the photocatalytic mechanism of the homojunction is more analogous to the Z-scheme mechanism [10,15]. The holes generated on the VB of PDI-g-C$_3$N$_4$ will therefore directly participate in the oxidation
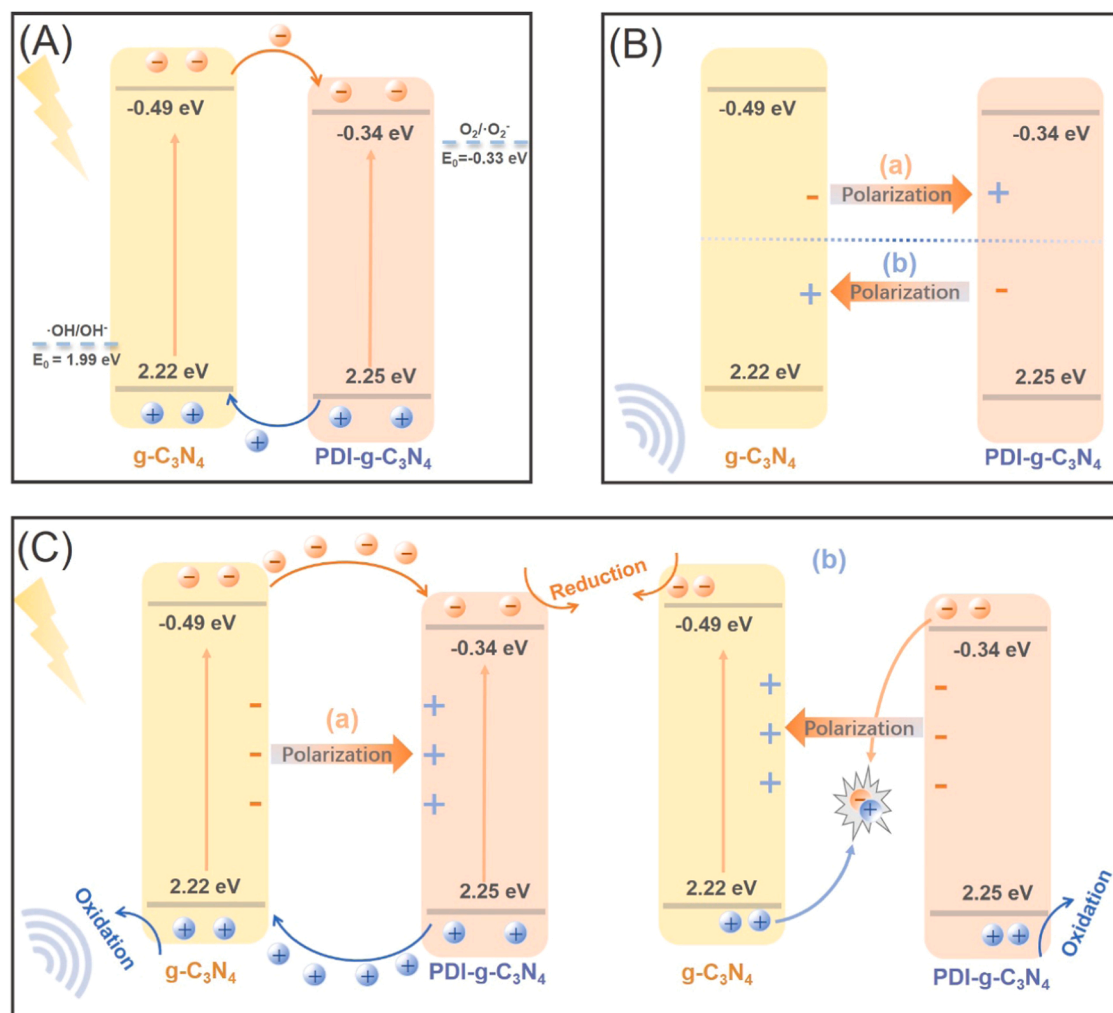
Scheme 1. Schematic diagram showing the mechanism of the individual (A) photocatalysis, (B) piezocatalysis, and (C) synergetic piezo-photocatalysis under different polarization directions.

reaction, rather than migrate to the VB of g-C$_3$N$_4$. Meanwhile, the photoexcited electrons in the CB of PDI-g-C$_3$N$_4$ will be driven by the build-in piezoelectric field and migrate to the g-C$_3$N$_4$ interfaces and combine with the photogenerated holes of the g-C$_3$N$_4$. There is a similar process in g-C$_3$N$_4$, where the photogenerated holes of g-C$_3$N$_4$ will recombine directly with the photoexcited electrons of PDI-g-C$_3$N$_4$, while its photoexcited electrons can migrate to the CB. Due to the polarization-induced piezoelectric field, the electrons cannot transfer to the PDI-g-C$_3$N$_4$ even if more positive CB potential. Hence the reduction reaction will also occur in situ. Therefore, despite the variable direction of polarization, the overall efficiency of the system is significantly enhanced [58].

3.4.3. Degradation pathways and toxicity assessment of the intermediates

The piezo-photocatalytic degradation pathway pathways of ATZ by the CNPC homojunction were analyzed via the LC-MS (Fig. S10-15). Fig. 8 shows the mass spectra of the samples at different reaction times. It is obvious that during the dark reaction process, the ATZ abundance (at $m/z = 216$) was unchanged, while once the ultrasonication and the visible light irradiation were applied, its abundance significantly decreased. Similarly, there were few intermediates-peaks shown during the dark reaction. Upon the catalysis began, the intermediates peaks increased gradually with the decrease of the ATZ. The major intermediates are speculated via the m/z peaks and the previous studies (Table S1).
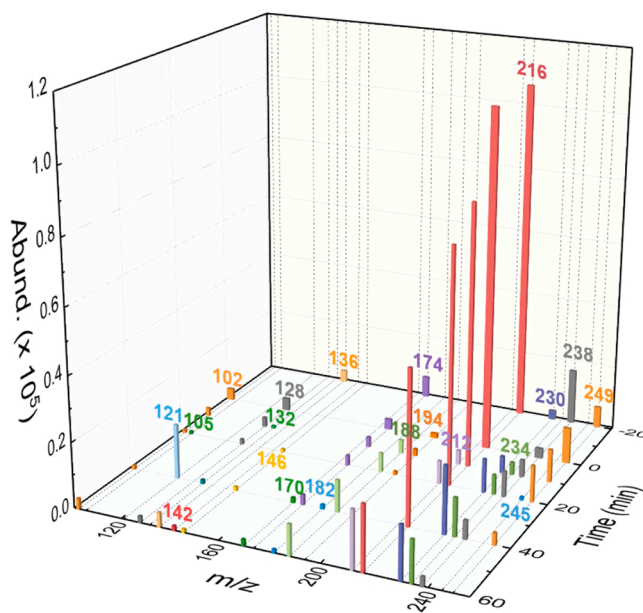

Fig. 8. The mass spectra change along the different reaction times.

According to the MS spectra changes, three possible degradation pathways of ATZ are proposed (Fig. 9A), and the intermediates abundance changes of each pathway were plotted (Fig. 9B-C). The relative abundance of the intermediates from the pathway I was the highest. In pathway I, serials oxidation was firstly occurring to the ATZ to produce convertible A1 and A2 with ketone and hydroxyl on the side chain [2, 83]. Subsequently, demethylation and hydroxylation were successive happened to produce A3–4 [9], before shortening the brunched chains and transforming to the A5–6 [2]. In pathway II, the hydroxylation on the side chain was also the first step for the production of B1, before the replacement of the chlorine by hydroxyl to form the B2 [84]. The hydroxyl on the brunched chain was then oxidized to ketone in B3 [9], before totally being removed from the amino groups and transformed to B4 [83,85,86]. Then the amino groups on the triazine ring were successively substituted by hydroxyl in B5, before the addition reaction and the ring-opening occurring on the triazine ring to produce B6–7 [87]. Comparatively, the intermediates abundance of the pathway III was the lowest, indicating this pathway was not favorable in the CNPC homojunction induced piezo-photocatalysis system. In pathway III, the chlorine on the triazine ring was firstly replaced by the methyl group to generate C1 ($m/z = 196$) [2]. Then, serials demethylation and hydroxylation occurred and the C3-C4 therefore formed [88]. Finally, the C5 was further produced by ring-opening and then transformed into C6 [88]. It is worth mentioning that the abundance of C5 was much higher than other intermediates in pathway 3. Given the complexity of the intermediate transforming process in the system, the intermediates in each pathway were also possible to undergo mutual transformation. Thus, it is possible for the C5 generated in other pathways by the ring-opening reaction. Finally, these intermediates may be further mineralized and transformed into CO_2, H_2O, and NO_3^- [86,88]. The ATZ mannerization extent in this system was further assessed via the TOC analysis (Fig. S16). After 60-min piezo-photocatalysis, the solution TOC content significantly decreased to only 28.7% of the 10 ppm ATZ, achieving a 71.3% TOC removal rate. The high TOC removal efficiency implies the outstanding mineralization ability of the CNPC/piezo-photocatalysis system, which is helpful for the toxicity reduction of the contaminant.

To thoroughly assess the toxicity of the intermediates produced during the piezo-photocatalytic process, the Toxicity Estimation Software Tool (TEST) with a consensus method was applied to predict the acute toxicity, bioaccumulation factor, developmental toxicity, and mutagenicity of the intermediates and to compare with ATZ (detailed information are shown in Table S2). Fig. 10 shows the acute toxicity of the intermediates to fathead minnow and rat by TEST, where the higher value indicates the lesser acute toxicity. The ATZ was the most hazardous to the fathead minnow, with the lowest LC_{50} (50% lethal concentration), and its LD_{50} (50% lethal amount) only higher than C2, C5, and C6. According to Globally Harmonized System of Classification and Labelling of Chemicals (GHS), the results can be classified as toxic (LC_{50} < 10, LD_{50} < 300), harmful ($10 < LC_{50} < 20$, $300 < LD_{50} < 2000$), and may be harmful ($20 < LC_{50}$, $2000 < LD_{50}$). Excepting the ATZ was harmful to the fathead minnow, all the intermediates are classified as 'may be harmful'. Comparatively, the intermediates are more harmful to oral rat, only B3–6 and C4 are classified as 'may be harmful'. After degradation, the bioaccumulation factors of the major intermediates are lowered, indicating they are less likely to be accumulated in organisms [89]. Similarly, the end-intermediates (A4, A6, B2, B7, C5) are non-developmental toxicants, indicating the effective toxicity reduction of the ATZ. Additionally, the mutagenicity results show that excepting C5, other intermediates are mutagenicity negative. Overall, the piezo-photocatalytic degradation of ATZ by the CNPC homojunction can effectively remove the ATZ and produce less harmful or non-harmful productions.
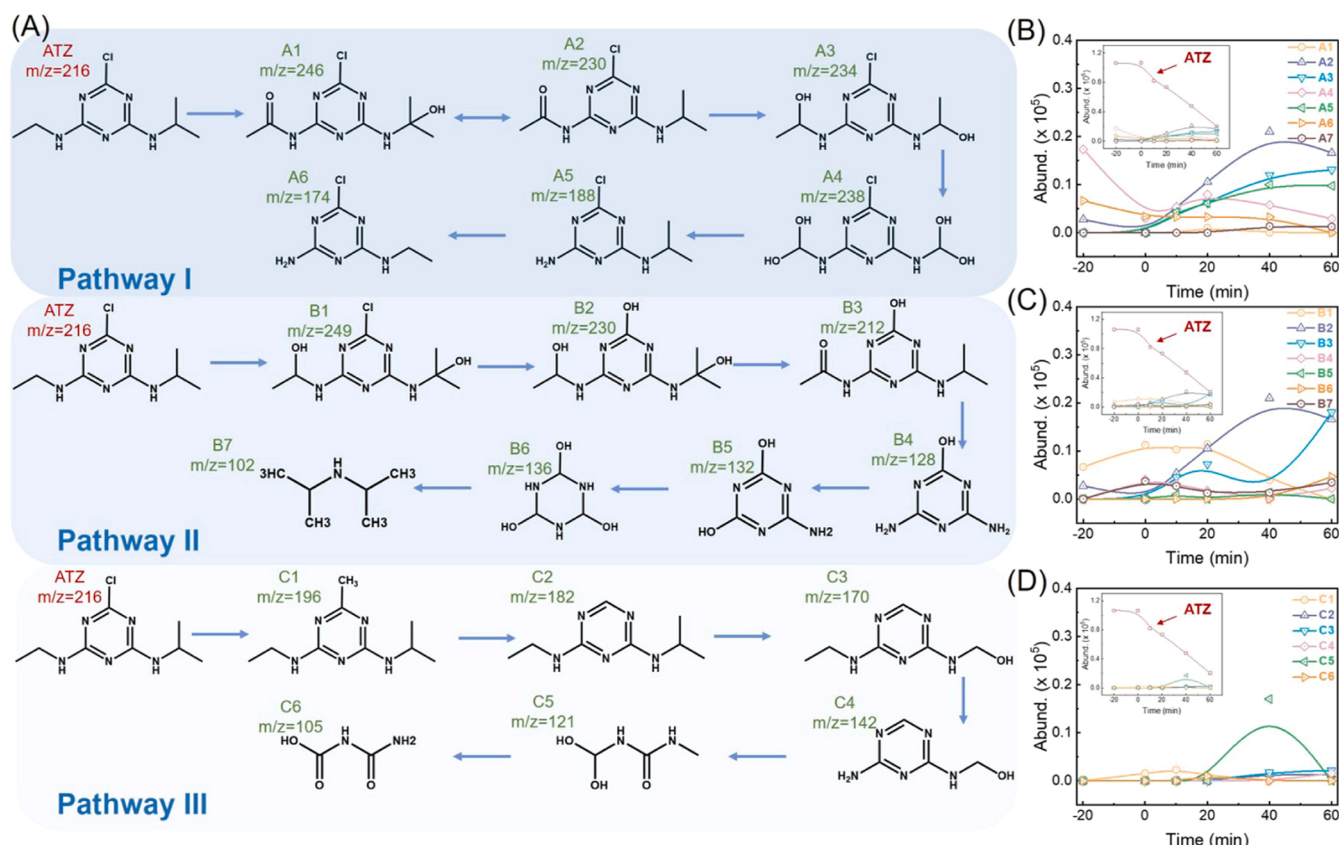

Fig. 9. (A) The proposed three pathways and (B-D) the corresponding intermediates abundance change.
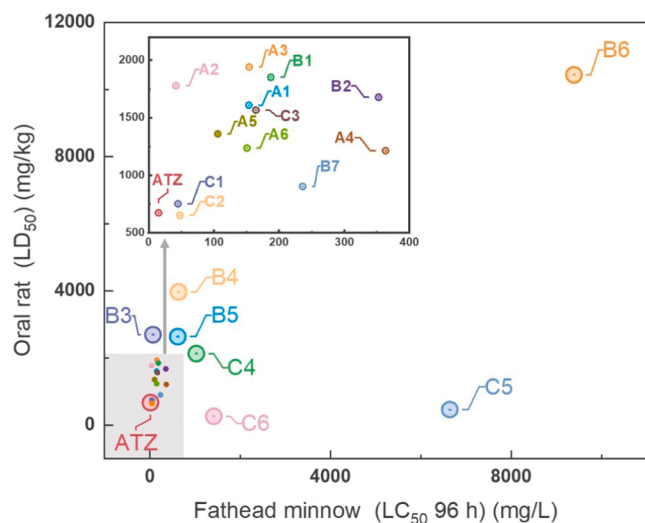
Fig. 10. The T.E.S.T. results evaluated the toxicity of the intermediates to the fathead minnow. and rats. Inset showed the enlarged detailed information in the gray area.

4. Conclusion

In summary, a novel g-C$_3$N$_4$/PDI-g-C$_3$N$_4$ homojunction with a thinner and porous layered structure and was fabricated via facile thermal condensation and successfully applied for piezo-photocatalytic ATZ degradation. With the optimized condition (pH=2.97), the homojunction even achieved 94% ATZ degradation. The homojunction can also generate 642.54 μM H$_2$O$_2$ within a 60-min piezo-photocatalysis. To in-depth understand the piezo-photocatalytic mechanism of the catalyst, reactive species analysis was carried out via quenching experiments and the ESR test. It was found that $^1O_2$, $\cdot O_2^-$, h$^+$, and ● OH are contributed to the ATZ degradation. In addition, the LC-MS was applied to analyze the ATZ degradation pathways and the intermediates. More than 20 intermediates and three degradation pathways were proposed with the serials of hydroxylation, ring-opening, and demethylation of ATZ. Meanwhile, the potential toxicity estimation of the intermediates was carried out via the TEST, implying the excellent toxicity reduction effect of the system. Hopefully, the design of such a powerful piezo-photocatalyst can offer more inspiration for environmental protection.

CRediT authorship contribution statement

Rongdi Tang: Conceptualization, Validation, Methodology, Investigation, Writing – original draft. **Daoxin Gong**: Supervision, Writing – review & editing. **Yaoyu Zhou:** Investigation, Writing – review & editing. **Yaocheng Deng**: Supervision, Writing – review & editing, Funding acquisition. **Chengyang Feng:** Investigation, Writing – review & editing. **Sheng Xiong**: Investigation, Writing – review & editing. **Ying Huang**: Investigation, Writing – review & editing. **Guanwei Peng:** Investigation, Writing – review & editing. **Ling Li**: Investigation, Writing – review & editing.

Declaration of Competing Interest

The authors declare that they have no known competing financial interests or personal relationships that could have appeared to influence the work reported in this paper.

Acknowledgments

Appendix A. Supporting information

Supplementary data associated with this article can be found in the online version at doi:10.1016/j.apcatb.2021.120929.

References

[1] Y.H. Guan, J. Ma, Y.M. Ren, Y.L. Liu, J.Y. Xiao, L.Q. Lin, C. Zhang, Efficient degradation of atrazine by magnetic porous copper ferrite catalyzed peroxymonosulfate oxidation via the formation of hydroxyl and sulfate radicals, Water Res. 47 (2013) 5431–5438.

[2] Y. Huang, C. Han, Y. Liu, M.N. Nadagouda, L. Machala, K.E. O'Shea, V.K. Sharma, D.D. Dionysiou, Degradation of atrazine by Zn$_x$Cu$_{1−x}$Fe$_2$O$_4$ nanomaterial-catalyzed sulfite under UV–vis light irradiation: green strategy to generate SO$_4$·$^-$, Appl. Catal. B 221 (2018) 380–392.

[3] E. Nyankson, J.K. Efavi, B. Agyei-Tuffour, G. Manu, Synthesis of TiO$_2$–Ag$_3$PO$_4$ photocatalyst material with high adsorption capacity and photocatalytic activity: application in the removal of dyes and pesticides, RSC Adv. 11 (2021) 17032–17045.

[4] R. Keyikoglu, O. Karatas, A. Khataee, M. Kobya, O.T. Can, R. Darvishi Cheshmeh Soltani, M. Isleyen, Peroxydisulfate activation by in-situ synthesized Fe$_3$O$_4$ nanoparticles for degradation of atrazine: performance and mechanism, Sep. Purif. Technol. 247 (2020), 116925.

[5] L. Zhang, H. Tian, R. Hong, C. Wang, Y. Wang, A. Peng, C. Gu, Photodegradation of atrazine in the presence of indole-3-acetic acid and natural montmorillonite clay minerals, Environ. Pollut. 240 (2018) 793–801.

[6] W.-K. Jo, N.C.S. Selvam, Z-scheme CdS/g-C$_3$N$_4$ composites with RGO as an electron mediator for efficient photocatalytic H$_2$ production and pollutant degradation, Chem. Eng. J. 317 (2017) 913–924.

[7] R. Tang, D. Gong, Y. Deng, S. Xiong, J. Deng, L. Li, Z. Zhou, J. Zheng, L. Su, L. Yang, π-π stacked step-scheme PDI/g-C$_3$N$_4$/TiO$_2$@Ti$_3$C$_2$ photocatalyst with enhanced visible photocatalytic degradation towards atrazine via peroxymonosulfate activation, Chem. Eng. J. 427 (2022), 131809.

[8] H.J. Choi, D. Kim, T.J. Lee, Photochemical degradation of atrazine in UV and UV/H$_2$O$_2$ process: pathways and toxic effects of products, J. Environ. Sci. Health B 48 (2013) 927–934.

[9] Z. Feng, Q. Tian, Q. Yang, Y. Zhou, H. Zhao, G. Zhao, Selectively photoelectrocatalytic reduction of oxygen to hydroxyl radical and singlet oxygen: mechanism and validation in coal wastewater, Appl. Catal. B 286 (2021), 119908.

[10] X. Huang, R. Lei, J. Yuan, F. Gao, C. Jiang, W. Feng, J. Zhuang, P. Liu, Insight into the piezo-photo coupling effect of PbTiO$_3$/CdS composites for piezo-photocatalytic hydrogen production, Appl. Catal. B 282 (2021), 119586.

[11] L. Wang, L. Xie, W. Zhao, S. Liu, Q. Zhao, Oxygen-facilitated dynamic active-site generation on strained MoS$_2$ during photo-catalytic hydrogen evolution, Chem. Eng. J. 405 (2021), 127028.

[12] S. Tu, Y. Guo, Y. Zhang, C. Hu, T. Zhang, T. Ma, H. Huang, Piezocatalysis and piezo-photocatalysis: catalysts classification and modification strategy, reaction mechanism, and practical application, Adv. Funct. Mater. 30 (2020), 2005158.

[13] S. Li, Z. Zhao, J. Zhao, Z. Zhang, X. Li, J. Zhang, Recent advances of ferro-, piezo-, and pyroelectric nanomaterials for catalytic applications, ACS Appl. Nano Mater. 3 (2020) 1063–1079.

[14] C. Hu, S. Tu, N. Tian, T. Ma, Y. Zhang, H. Huang, Photocatalysis enhanced by external fields, Angew. Chem. Int Ed. Engl. 60 (2021) 16309–16328.

[15] C. Hu, F. Chen, Y. Wang, N. Tian, T. Ma, Y. Zhang, H. Huang, Exceptional cocatalyst-free photo-enhanced piezocatalytic hydrogen evolution of carbon nitride nanosheets from strong in-plane polarization, Adv. Mater. (2021), e2101751.

[16] F. Chen, Z. Ma, L. Ye, T. Ma, T. Zhang, Y. Zhang, H. Huang, Macroscopic spontaneous polarization and surface oxygen vacancies collaboratively boosting CO$_2$ photoreduction on BiOIO$_3$ single crystals, Adv. Mater. 32 (2020), e1908350.

[17] D. Liu, Y. Song, Z. Xin, G. Liu, C. Jin, F. Shan, High-piezocatalytic performance of eco-friendly (Bi$_{1/2}$Na$_{1/2}$)TiO$_3$-based nanofibers by electrospinning, Nano Energy 65 (2019), 104024.

[18] M. Pan, S. Liu, J.W. Chew, Unlocking the high redox activity of MoS$_2$ on dual-doped graphene as a superior piezocatalyst, Nano Energy 68 (2020), 104366.

[19] W. Feng, J. Yuan, F. Gao, B. Weng, W. Hu, Y. Lei, X. Huang, L. Yang, J. Shen, D. Xu, X. Zhang, P. Liu, S. Zhang, Piezopotential-driven simulated electrocatalytic nanosystem of ultrasmall MoC quantum dots encapsulated in ultrathin N-doped graphene vesicles for superhigh H$_2$ production from pure water, Nano Energy 75 (2020), 104990.

[20] R. Tang, D. Gong, Y. Deng, S. Xiong, J. Zheng, L. Li, Z. Zhou, L. Su, J. Zhao, π-π stacking derived from graphene-like biochar/g-C$_3$N$_4$ with tunable band structure for photocatalytic antibiotics degradation via peroxymonosulfate activation, J. Hazard. Mater. 423 (2021), 126944.

[21] J. Wang, D. Liu, Y. Zhu, S. Zhou, S. Guan, Supramolecular packing dominant photocatalytic oxidation and anticancer performance of PDI, Appl. Catal. B 231 (2018) 251–261.

[22] J. Yang, H. Miao, J. Jing, Y. Zhu, W. Choi, Photocatalytic activity enhancement of PDI supermolecular via π-π action and energy level adjusting with graphene quantum dots, Appl. Catal. B 281 (2021), 119547.

[23] D. Liu, J. Wang, X. Bai, R. Zong, Y. Zhu, Self-assembled PDINH supramolecular system for photocatalysis under visible light, Adv. Mater. 28 (2016) 7284–7290.

[24] C. Hu, Y.H. Lin, M. Yoshida, S. Ashimura, Influence of phosphorus doping on triazole-based g-C₃N₅ nanosheets for enhanced photoelectrochemical and photocatalytic performance, ACS Appl. Mater. Interfaces 13 (2021) 24907–24915.

[25] C. Feng, L. Tang, Y. Deng, J. Wang, W. Tang, Y. Liu, Z. Chen, J. Yu, J. Wang, Q. Liang, Synthesis of branched WO₃@W₁₈O₄₉ homojunction with enhanced interfacial charge separation and full-spectrum photocatalytic performance, Chem. Eng. J. 389 (2020), 124474.

[26] P. Li, Y. Zhou, Z. Zhao, Q. Xu, X. Wang, M. Xiao, Z. Zou, Hexahedron prism-anchored octahedronal CeO₂: crystal facet-based homojunction promoting efficient solar fuel synthesis, J. Am. Chem. Soc. 137 (2015) 9547–9550.

[27] X. Wang, Q. Xu, M. Li, S. Shen, X. Wang, Y. Wang, Z. Feng, J. Shi, H. Han, C. Li, Photocatalytic overall water splitting promoted by an alpha-beta phase junction on Ga₂O₃, Angew. Chem. Int Ed. Engl. 51 (2012) 13089–13092.

[28] S.M. Wu, X.L. Liu, X.L. Lian, G. Tian, C. Janiak, Y.X. Zhang, Y. Lu, H.Z. Yu, J. Hu, H. Wei, H. Zhao, G.G. Chang, G. Van Tendeloo, L.Y. Wang, X.Y. Yang, B.L. Su, Homojunction of oxygen and titanium vacancies and its interfacial n-p effect, Adv. Mater. 30 (2018), e1802173.

[29] G. Liu, G. Zhao, W. Zhou, Y. Liu, H. Pang, H. Zhang, D. Hao, X. Meng, P. Li, T. Kako, J. Ye, In situ bond modulation of graphitic carbon nitride to construct p-n homojunctions for enhanced photocatalytic hydrogen production, Adv. Funct. Mater. 26 (2016) 6822–6829.

[30] Y. Jin, D.H. Keum, S.J. An, J. Kim, H.S. Lee, Y.H. Lee, A van der Waals homojunction: Ideal p-n diode behavior in MoSe₂, Adv. Mater. 27 (2015) 5534–5540.

[31] C. Yang, Q. Tan, Q. Li, J. Zhou, J. Fan, B. Li, J. Sun, K. Lv, 2D/2D Ti₃C₂ MXene/g-C₃N₄ nanosheets heterojunction for high efficient CO₂ reduction photocatalyst: dual effects of urea, Appl. Catal. B 268 (2020), 118738.

[32] S. Chu, Y. Wang, Y. Guo, J. Feng, C. Wang, W. Luo, X. Fan, Z. Zou, Band structure engineering of carbon nitride: In search of a polymer photocatalyst with high photooxidation roperty, ACS Catal. 3 (2013) 912–919.

[33] Y. Li, Y. Fang, Z. Cao, N. Li, D. Chen, Q. Xu, J. Lu, Construction of g-C₃N₄/PDI@ MOF heterojunctions for the highly efficient visible light-driven degradation of pharmaceutical and phenolic micropollutants, Appl. Catal. B 250 (2019) 150–162.

[34] Y. Kofuji, Y. Isobe, Y. Shiraishi, H. Sakamoto, S. Ichikawa, S. Tanaka, T. Hirai, Hydrogen peroxide production on a carbon nitride–boron nitride-reduced graphene oxide hybrid photocatalyst under visible light, ChemCatChem 10 (2018) 2070–2077.

[35] O. Tomita, T. Otsubo, M. Higashi, B. Ohtani, R. Abe, Partial oxidation of alcohols on visible-light-responsive WO₃ photocatalysts loaded with palladium oxide cocatalyst, ACS Catal. 6 (2016) 1134–1144.

[36] Y. Jiang, Z. Lin, Y. Zhang, Y. Lai, D. Liang, C. Yang, Facile synthesis of porous C-doped C₃N₄: Fast charge separation and enhanced photocatalytic hydrogen evolution, N. J. Chem. 44 (2020) 17891–17898.

[37] Z. Xiong, Y. Wang, M. Muthu, Y. Zhang, Construction of an in-situ Fenton-like system based on a g-C₃N₄ composite photocatalyst, J. Hazard. Mater. 373 (2019) 565–571.

[38] D.G. Papageorgiou, I.A. Kinloch, R.J. Young, Mechanical properties of graphene and graphene-based nanocomposites, Prog. Mater. Sci. 90 (2017) 75–127.

[39] F. Han, S. Luo, L. Xie, J. Zhu, W. Wei, X. Chen, F. Liu, W. Chen, J. Zhao, L. Dong, K. Yu, X. Zeng, F. Rao, L. Wang, Y. Huang, Boosting the yield of MXene 2D sheets via a facile hydrothermal-assisted intercalation, ACS Appl. Mater. Interfaces 11 (2019) 8443–8452.

[40] Y. Deng, C. Feng, L. Tang, Y. Zhou, Z. Chen, H. Feng, J. Wang, J. Yu, Y. Liu, Ultrathin low dimensional heterostructure composites with superior photocatalytic activity: Insight into the multichannel charge transfer mechanism, Chem. Eng. J. 393 (2020), 124718.

[41] C. Feng, L. Tang, Y. Deng, G. Zeng, J. Wang, Y. Liu, Z. Chen, J. Yu, J. Wang, Enhancing optical absorption and charge transfer: synthesis of S-doped h-BN with tunable band structures for metal-free visible-light-driven photocatalysis, Appl. Catal. B 256 (2019), 117827.

[42] G.P. Mane, S.N. Talapaneni, K.S. Lakhi, H. Ilbeygi, U. Ravon, K. Al-Bahily, T. Mori, D.H. Park, A. Vinu, Highly ordered nitrogen-rich mesoporous carbon nitrides and their superior performance for sensing and photocatalytic hydrogen generation, Angew. Chem. Int Ed. Engl. 56 (2017) 8481–8485.

[43] Q. Gao, J. Xu, Z. Wang, Y. Zhu, Enhanced visible photocatalytic oxidation activity of perylene diimide/g-C₃N₄ n-n heterojunction via π-π interaction and interfacial charge separation, Appl. Catal. B 271 (2020), 118933.

[44] Y. Deng, L. Tang, C. Feng, G. Zeng, J. Wang, Y. Lu, Y. Liu, J. Yu, S. Chen, Y. Zhou, Construction of plasmonic Ag and nitrogen-doped graphene quantum dots codecorated ultrathin graphitic carbon nitride nanosheet composites with enhanced photocatalytic activity: Full-spectrum response ability and mechanism insight, ACS Appl. Mater. Interfaces 9 (2017) 42816–42828.

[45] Z. Ai, Y. Shao, B. Chang, B. Huang, Y. Wu, X. Hao, Effective orientation control of photogenerated carrier separation via rational design of a Ti₃C₂(TiO₂)@CdS/MoS₂ photocatalytic system, Appl. Catal. B 242 (2019) 202–208.

[46] W. Yu, J. Chen, T. Shang, L. Chen, L. Gu, T. Peng, Direct Z-scheme g-C₃N₄/WO₃ photocatalyst with atomically defined junction for H₂ production, Appl. Catal. B 219 (2017) 693–704.

[47] F. Xu, K. Meng, B. Zhu, H. Liu, J. Xu, J. Yu, Graphdiyne: a new photocatalytic CO₂ reduction cocatalyst, Adv. Funct. Mater. 29 (2019), 1904256.

[48] M. Yu, S. Zhou, Z. Wang, J. Zhao, J. Qiu, Boosting electrocatalytic oxygen evolution by synergistically coupling layered double hydroxide with MXene, Nano Energy 44 (2018) 181–190.

[49] Y. Deng, L. Tang, G. Zeng, C. Feng, H. Dong, J. Wang, H. Feng, Y. Liu, Y. Zhou, Y. Pang, Plasmonic resonance excited dual Z-scheme BiVO₄/Ag/Cu₂O nanocomposite: synthesis and mechanism for enhanced photocatalytic performance in recalcitrant antibiotic degradation, Environ. Sci. Nano 4 (2017) 1494–1511.

[50] Y. Deng, L. Tang, C. Feng, G. Zeng, Z. Chen, J. Wang, H. Feng, B. Peng, Y. Liu, Y. Zhou, Insight into the dual-channel charge-charrier transfer path for nonmetal plasmonic tungsten oxide based composites with boosted photocatalytic activity under full-spectrum light, Appl. Catal. B 235 (2018) 225–237.

[51] Y. Deng, L. Tang, G. Zeng, Z. Zhu, M. Yan, Y. Zhou, J. Wang, Y. Liu, J. Wang, Insight into highly efficient simultaneous photocatalytic removal of Cr(VI) and 2,4-diclorophenol under visible light irradiation by phosphorus doped porous ultrathin g-C₃N₄ nanosheets from aqueous media: performance and reaction mechanism, Appl. Catal. B 203 (2017) 343–354.

[52] R. Tang, S. Xiong, D. Gong, Y. Deng, Y. Wang, L. Su, C. Ding, L. Yang, C. Liao, Ti₃C₂ 2D MXene: recent progress and perspectives in photocatalysis, ACS Appl. Mater. Interfaces 12 (2020) 56663–56680.

[53] X. Han, L. An, Y. Hu, Y. Li, C. Hou, H. Wang, Q. Zhang, Ti₃C₂ MXene-derived carbon-doped TiO₂ coupled with g-C₃N₄ as the visible-light photocatalysts for photocatalytic H₂ generation, Appl. Catal. B 265 (2020), 118539.

[54] Q. Liang, X. Liu, J. Wang, Y. Liu, Z. Liu, L. Tang, B. Shao, W. Zhang, S. Gong, M. Cheng, Q. He, C. Feng, In-situ self-assembly construction of hollow tubular g-C₃N₄ isotype heterojunction for enhanced visible-light photocatalysis: Experiments and theories, J. Hazard. Mater. 401 (2021), 123355.

[55] C. Zhang, W. Fei, H. Wang, N. Li, D. Chen, Q. Xu, H. Li, J. He, J. Lu, p-n Heterojunction of BiOI/ZnO nanorod arrays for piezo-photocatalytic degradation of bisphenol A in water, J. Hazard. Mater. 399 (2020), 123109.

[56] Z. Liu, L. Wang, X. Yu, J. Zhang, R. Yang, X. Zhang, Y. Ji, M. Wu, L. Deng, L. Li, Z. L. Wang, Piezoelectric-effect-enhanced full-spectrum photoelectrocatalysis in p–n heterojunction, Adv. Funct. Mater. 29 (2019), 1807279.

[57] L. Pan, S. Sun, Y. Chen, P. Wang, J. Wang, X. Zhang, J.J. Zou, Z.L. Wang, Advances in piezo-phototronic effect enhanced photocatalysis and photoelectrocatalysis, Adv. Energy Mater. 10 (2020), 2000214.

[58] C.-Y. Tu, J.M. Wu, Localized surface plasmon resonance coupling with piezophototronic effect for enhancing hydrogen evolution reaction with Au@MoS₂ nanoflowers, Nano Energy (2021), 106131.

[59] J. Wang, W. Shi, D. Liu, Z. Zhang, Y. Zhu, D. Wang, Supramolecular organic nanofibers with highly efficient and stable visible light photooxidation performance, Appl. Catal. B 202 (2017) 289–297.

[60] E.M. Samsudin, S.B. Abd Hamid, J.C. Juan, W.J. Basirun, A.E. Kandjani, S. K. Bhargava, Controlled nitrogen insertion in titanium dioxide for optimal photocatalytic degradation of atrazine, RSC Adv. 5 (2015) 44041–44052.

[61] T.S. Jamil, H.A. Abbas, R.A. Nasr, R.N. Vannier, Visible light activity of BaFe₁₋ₓCuₓO₃₋δ as photocatalyst for atrazine degradation, Ecotoxicol. Environ. Saf. 163 (2018) 620–628.

[62] Y. Xue, P. Wang, C. Wang, Y. Ao, Efficient degradation of atrazine by BiOBr/UiO-66 composite photocatalyst under visible light irradiation: environmental factors, mechanisms and degradation pathways, Chemosphere 203 (2018) 497–505.

[63] J.M. Dangwang Dikdim, Y. Gong, G.B. Noumi, J.M. Sielechi, X. Zhao, N. Ma, M. Yang, J.B. Tchatchueng, Peroxymonosulfate improved photocatalytic degradation of atrazine by activated carbon/graphitic carbon nitride composite under visible light irradiation, Chemosphere 217 (2019) 833–842.

[64] S.M. Chen, N. Lu, J.Y. Chen, C.Y. Yang, Y.P. Yeh, T.Y. Feng, Y.H. Shih, T. Kokulnathan, D. Chen, Enhanced photocatalytic degradation of atrazine by platinized titanium dioxide under 352 nm irradiation, Water Sci. Technol. 75 (2017) 1128–1137.

[65] H.X. Wang, L.N. Zhu, F.Q. Guo, Photoelectrocatalytic degradation of atrazine by boron-fluorine Co-doped TiO₂ nanotube arrays, Environ. Sci. Pollut. Res. Int. 26 (2019) 33847–33855.

[66] M.L. Yola, T. Eren, N. Atar, A novel efficient photocatalyst based on TiO₂ nanoparticles involved boron enrichment waste for photocatalytic degradation of atrazine, Chem. Eng. J. 250 (2014) 288–294.

[67] J. Andersen, M. Pelaez, L. Guay, Z. Zhang, K. O'Shea, D.D. Dionysiou, NF-TiO₂ photocatalysis of amitrole and atrazine with addition of oxidants under simulated solar light: emerging synergies, degradation intermediates, and reusable attributes, J. Hazard. Mater. 260 (2013) 569–575.

[68] S. Klementova, M. Zlamal, Photochemical degradation of triazine herbicides - comparison of homogeneous and heterogeneous photocatalysis, Photochem. Photobiol. Sci. 12 (2013) 660–663.

[69] Q. Liang, X. Liu, B. Shao, L. Tang, Z. Liu, W. Zhang, S. Gong, Y. Liu, Q. He, T. Wu, Y. Pan, S. Tong, Construction of fish-scale tubular carbon nitride-based heterojunction with boosting charge separation in photocatalytic tetracycline degradation and H₂O₂ production, Chem. Eng. J. 426 (2021), 130831.

[70] J.H. Lee, H. Cho, S.O. Park, J.M. Hwang, Y. Hong, P. Sharma, W.C. Jeon, Y. Cho, C. Yang, S.K. Kwak, H.R. Moon, J.-W. Jang, High performance H₂O₂ production achieved by sulfur-doped carbon on CdS photocatalyst via inhibiting reverse H₂O₂ decomposition, Appl. Catal. B 284 (2021), 119690.

[71] J. Du, C. Wang, Z. Zhao, F. Cui, Q. Ou, J. Liu, Role of oxygen and superoxide radicals in promoting H₂O₂ production during VUV/UV radiation of water, Chem. Eng. Sci. 241 (2021), 116683.

[72] J. Wang, C. Li, M. Rauf, H. Luo, X. Sun, Y. Jiang, Gas diffusion electrodes for H_2O_2 production and their applications for electrochemical degradation of organic pollutants in water: a review, Sci. Total Environ. 759 (2021) 143459.

[73] T. Cai, L. Wang, Y. Liu, S. Zhang, W. Dong, H. Chen, X. Yi, J. Yuan, X. Xia, C. Liu, S. Luo, Ag_3PO_4/Ti_3C_2 MXene interface materials as a schottky catalyst with enhanced photocatalytic activities and anti-photocorrosion performance, Appl. Catal. B 239 (2018) 545–554.

[74] Z. Zhao, J. Zhao, C. Yang, Efficient removal of ciprofloxacin by peroxymonosulfate/Mn_3O_4-MnO_2 catalytic oxidation system, Chem. Eng. J. 327 (2017) 481–489.

[75] S. Cao, B. Shen, T. Tong, J. Fu, J. Yu, 2D/2D heterojunction of ultrathin MXene/Bi_2WO_6 nanosheets for improved photocatalytic CO_2 reduction, Adv. Funct. Mater. 28 (2018), 1800136.

[76] Y. Qi, B. Ge, Y. Zhang, B. Jiang, C. Wang, M. Akram, X. Xu, Three-dimensional porous graphene-like biochar derived from Enteromorpha as a persulfate activator for sulfamethoxazole degradation: Role of graphitic N and radicals transformation, J. Hazard. Mater. 399 (2020), 123039.

[77] Y. Shi, J. Li, D. Wan, J. Huang, Y. Liu, Peroxymonosulfate-enhanced photocatalysis by carbonyl-modified g-C_3N_4 for effective degradation of the tetracycline hydrochloride, Sci. Total Environ. 749 (2020), 142313.

[78] H. Shao, X. Zhao, Y. Wang, R. Mao, Y. Wang, M. Qiao, S. Zhao, Y. Zhu, Synergetic activation of peroxymonosulfate by Co_3O_4 modified g-C_3N_4 for enhanced degradation of diclofenac sodium under visible light irradiation, Appl. Catal. B 218 (2017) 810–818.

[79] H. Hou, X. Zeng, X. Zhang, Production of hydrogen peroxide by photocatalytic processes, Angew. Chem. Int Ed. Engl. 59 (2020) 17356–17376.

[80] A.Y. Zhang, Y.Y. He, T. Lin, N.H. Huang, Q. Xu, J.W. Feng, A simple strategy to refine Cu_2O photocatalytic capacity for refractory pollutants removal: Roles of oxygen reduction and Fe(II) chemistry, J. Hazard. Mater. 330 (2017) 9–17.

[81] M. Duan, L. Jiang, B. Shao, C. Feng, H. Yu, H. Guo, H. Chen, W. Tang, Enhanced visible-light photocatalytic degradation activity of Ti_3C_2/PDIsm via π–π interaction and interfacial charge separation: experimental and theoretical investigations, Appl. Catal. B 297 (2021), 120439.

[82] X. Lian, W. Xue, S. Dong, E. Liu, H. Li, K. Xu, Construction of S-scheme Bi_2WO_6/g-C_3N_4 heterostructure nanosheets with enhanced visible-light photocatalytic degradation for ammonium dinitramide, J. Hazard. Mater. 412 (2021), 125217.

[83] G. Ye, P. Luo, Y. Zhao, G. Qiu, Y. Hu, S. Preis, C. Wei, Three-dimensional Co/Ni bimetallic organic frameworks for high-efficient catalytic ozonation of atrazine: Mechanism, effect parameters, and degradation pathways analysis, Chemosphere 253 (2020), 126767.

[84] X. Dong, B. Ren, X. Zhang, X. Liu, Z. Sun, C. Li, Y. Tan, S. Yang, S. Zheng, D. D. Dionysiou, Diatomite supported hierarchical 2D $CoNi_3O_4$ nanoribbons as highly efficient peroxymonosulfate catalyst for atrazine degradation, Appl. Catal. B 272 (2020), 118971.

[85] S.Q. Tian, J.Y. Qi, Y.P. Wang, Y.L. Liu, L. Wang, J. Ma, Heterogeneous catalytic ozonation of atrazine with Mn-loaded and Fe-loaded biochar, Water Res. 193 (2021), 116860.

[86] N. Yang, Y. Liu, J. Zhu, Z. Wang, J. Li, Study on the efficacy and mechanism of Fe-TiO_2 visible heterogeneous Fenton catalytic degradation of atrazine, Chemosphere 252 (2020), 126333.

[87] C. Li, Y. Huang, X. Dong, Z. Sun, X. Duan, B. Ren, S. Zheng, D.D. Dionysiou, Highly efficient activation of peroxymonosulfate by natural negatively-charged kaolinite with abundant hydroxyl groups for the degradation of atrazine, Appl. Catal. B 247 (2019) 10–23.

[88] Z. Shen, H. Zhou, Z. Pan, Y. Guo, Y. Yuan, G. Yao, B. Lai, Degradation of atrazine by Bi_2MoO_6 activated peroxymonosulfate under visible light irradiation, J. Hazard. Mater. 400 (2020), 123187.

[89] J. Pan, B. Gao, P. Duan, K. Guo, X. Xu, Q. Yue, Recycling exhausted magnetic biochar with adsorbed Cu^{2+} as a cost-effective permonosulfate activator for norfloxacin degradation: Cu contribution and mechanism, J. Hazard. Mater. 413 (2021), 125413.